energies

MDPI

Article

Grid-Connected Photovoltaic Systems with Energy Storage for Ancillary Services

Luccas Tadeu Farnezes Soares [1], Arthur Costa de Souza [1], Waner Wodson Aparecido Gonçalves Silva [1,*], Luiz Felipe Pugliese [1] and Guilherme Henrique Alves [2]

[1] Institute of Technological Sciences, Federal University of Itajubá, Itabira Campus, Itabira 35903-087, MG, Brazil; luccastadeu@unifei.edu.br (L.T.F.S.); arthurcosta@unifei.edu.br (A.C.d.S.); pugliese@unifei.edu.br (L.F.P.)

[2] Faculty of Electrical Engineering, Federal University of Uberlândia, Uberlândia 38400-902, MG, Brazil; guilherme.henrique.alves@ufu.br

* Correspondence: waner@unifei.edu.br

Abstract: This paper presents the topology and control of a photovoltaic inverter with an internal battery storage system in conjunction with droop control designed to perform ancillary services such as frequency and reactive power support (voltage regulation), active power dispatch through a proposal to control the charging and discharging of batteries and harmonic current compensation (active filter) in a microgrid connected to an IEEE 13-bus system. The converter in question consists of two stages, a 3-level NPC DC/AC converter and Boost and Buck-Boost DC/DC converters. The system in question is capable of helping to dampen frequency oscillations, as well as regulating the PCC charging curve by charging or discharging the battery bank. In addition, the proposed system is capable of supplying reactive power to the grid on a permanent basis, thus helping with voltage control. It is also capable of compensating for harmonic currents caused by non-linear loads connected to the PCC. In this context, we can see the multifunctionality of the photovoltaic inverter in helping to mitigate disturbances associated with the power quality, with the differential of charge and discharge control to preserve the useful life of the energy storage system. For this study, Matlab/Simulink software was used to implement and validate the proposed topology and control systems. In the computer simulations carried out, satisfactory results were obtained in relation to the execution of the ancillary services mentioned above, thus demonstrating the viability of the proposed strategy.

Keywords: photovoltaic generation; frequency support; reactive power support; load curve regulation; harmonic compensation; energy storage system; battery system; power quality

check for updates

Citation: Soares, L.T.F.; de Souza, A.C.; Silva, W.W.A.G.; Pugliese, L.F.; Alves, G.H. Grid-Connected Photovoltaic Systems with Energy Storage for Ancillary Services. *Energies* **2023**, *16*, 7379. https://doi.org/10.3390/en16217379

Academic Editor: Alon Kuperman

Received: 1 October 2023
Revised: 26 October 2023
Accepted: 29 October 2023
Published: 31 October 2023

Copyright: © 2023 by the authors. Licensee MDPI, Basel, Switzerland. This article is an open access article distributed under the terms and conditions of the Creative Commons Attribution (CC BY) license (https://creativecommons.org/licenses/by/4.0/).

1. Introduction

In recent years, the composition of the energy matrix has experienced significant changes, mainly due to growing environmental concerns. The increasing integration of renewable resources into the power grid through DC-to-AC converters has introduced new challenges in the operation and control of electrical systems. The replacement of conventional synchronous generators by renewable energy sources has contributed to the reduction of the inertia of the system, making it more vulnerable to frequency fluctuations and resulting in the degradation of the dynamic response of the electrical system [1].

Because inertia restricts frequency oscillation after disturbances in the system, control measures become essential to ensure adequate frequency responses [2]. Several efforts were undertaken in proposing control strategies for wind and photovoltaic plants, aiming to improve the stability of the system. Synthetic or virtual inertia adds a frequency control contribution from sources such as wind farms and solar farms [3,4]. Energy storage represents another approach to intensifying frequency control in systems with low inertia [5].

Despite the steady increase in Distributed Generation (DG) connection by Renewable Energy Sources (RES), conventional synchronous generators will continue to play a significant role in power generation, especially in countries with vast water resources. The seasonal variability of renewable energy resources will impact the inertia of the electricity system as its contribution increases. This can result in the reduction or disconnection of conventional synchronous generators when RES generation is high, or in increasing the power of conventional generators and their reconnection when RES generation decreases. In the implementation of RES, it is possible to perform additional controls on the power converters to simulate a synthetic inertia, thus emulating the frequency response of the synchronous generators [6]. In addition, to improve the frequency response of the system, several approaches have been proposed, including direct estimation of inertia, adjustment of the parameters of conventional speed controllers, and the addition of supplementary controls to conventional speed control systems.

Microgrids are becoming a growing focus of research due to the reduction in costs associated with small-scale generation and batteries [7]. These microgrids can operate in two distinct modes: connected to the power grid or isolated. Similarly, voltage source converters (VSC) in microgrids can be categorized into two types: those that grid forming (voltage-controlled mode in isolated microgrids) and grid following (current-controlled mode in grid-connected microgrids) [8]. In the scenario where distributed generation (DG) units operate connected to the grid, they are usually controlled according to the frequency established by the power grid, and one of the most widely adopted control strategies for this configuration is discussed in [9]. However, there are situations in which voltage and frequency variations occur even when the power grid is connected, such as in weak grid (low level of short circuit) [10].

On the other hand, in island mode, the electronic power converter plays the role of interface between the loads and the sources of distributed generation, functioning as voltage sources. They are responsible for managing the power distribution between the DGs, according to the availability of active power from the primary source, while regulating and stabilizing the voltage and frequency [11]. Regarding the modes of operation of the converters in microgrids, there is an additional functionality called "grid conditioning mode". This mode can be applied both in the formation and in the monitoring of the grid. In this context, the electronic power converter also plays a crucial role in improving the power quality in various situations, such as:

- Reduction of harmonic content generated by nonlinear loads [12,13].
- Reactive power compensation for voltage regulation [11,14].
- Uninterruptible power supply to increase supply reliability [15].
- Correction of voltage sags and swells in critical loads [13,16].
- Power management through a battery system for peak demand reduction, load leveling, or peak consumption management [17].

In the context of island mode, control strategies are usually based on the "droop" principle [8]. In addition, there are integrated control approaches that involve hierarchical structures, typically comprising three levels of control: primary, secondary, and tertiary [18]. Primary control plays a key role in stabilizing voltage and frequency by providing a plug-and-play capability for distributed generation units (DGs) [11]. The secondary control, in turn, acts as a decentralized controller, correcting deviations in voltage and frequency to improve the power quality [18]. Tertiary control encompasses considerations about the optimal flow of energy throughout the microgrid or the interaction with the main grid.

Some research proposes the implementation of a "virtual synchronous machine" by means of electronic power converters, which allows the creation of a virtual inertia and the regulation of voltage and frequency. However, it's important to note that this approach tends to have slower dynamics compared to traditional droop control [18]. A multifunctional inverter can perform various functions under certain conditions, in order to maintain the stability and effectiveness of the system. However, some researchers have focused exclusively on some additional functions, such as: Refs. [19,20] propose that the

inverter perform the only extra function of voltage regulation; similarly Refs. [21,22] show the Volt/VAr capacity of the electronic converter as an intelligent/extra function; Ref. [23] proposed as a smooth transition from grid-connected mode to islanded mode on a microgrid as a multifunctional inverter; Ref. [24] showed reactive power compensation functionality to adjust the use of inverter nomenclature. For the present work, a multifunctional inverter is considered one that is capable of imposing functions according to the needs of the grid.

To date, there are few examples in the literature that explore the impacts of multifunctional inverters on the direct current (DC) side, encompassing renewable energy sources (RES) and battery energy storage systems (BESS), in order to effectively incorporate additional functionalities on the alternating current (AC) side [25]. These functionalities include harmonic compensation, steady-state voltage regulation, power factor correction, frequency stability support, and power dispatch optimization to keep the multifunctional inverter operating close to 1 pu. It is important to note that in most related research, the authors present analyses under stable state conditions (balanced and without harmonic ditortion in grid) and using simplifications of the DC side by considering it as a voltage source, as exemplified in the studies [7,26].

This paper focuses on the operation of a converter in both mains-connected and island mode in a microgrid. It explores the operation of a multifunctional inverter with internal energy storage through batteries that meets the specific demands of the power grid, covering:

- The islanding scenarios;
- The management of harmonics caused by the insertion of nonlinear loads;
- The provision of ancillary services of reactive support, frequency, and power dispatch for maintenance of the operating reserve;
- The execution of the energy management mode in hybrid systems (photovoltaic generation with batteries).

In this sense, the relevance of this research applies to in the computational implementation of a multifunctional converter that has the capacity to assist the grid in various contingency situations, with the aim of maintaining its operability, differently other proposals mentioned above which only solve a few specific disturbances. Also noteworthy is the good dynamic performance of the controls implemented in the DC-AC converter, which manage to improve power quality indicators without compromising photovoltaic generation.

The main contributions of this paper are summarized below:

- The development of the two-stage multifunctional inverter model with internal energy storage by means of a battery bank;
- Battery charge and discharge control strategy to contribute to voltage and frequency stability in conjunction with droop control;
- Modified active filter proposal that allows filtering harmonic orders of current;
- Ability to operate in islanded mode with a synchronous machine playing the role of grid forming in the IEEE 13-bus system.

Therefore, the aim of this research is to show that the multifunctional inverter is capable of operating in various grid contingencies and at the same time helping to mitigate the aforementioned power quality problems, together with the battery bank as an auxiliary source. In this context, the insertion of the storage system on the DC bus of the photovoltaic inverter aims to provide power dispatchability of the generating unit, since photovoltaic generation alone does not allow this control.

In addition, charge and discharge control enables frequency regulation in islanding situations and/or when there is an imbalance in the power (input or output of a significant load) of the PCC. Still on the subject of the proposed charge and discharge control, it makes it possible to manage the flow of battery charging power without reaching the phenomenon of deep discharge (a critical level of charge that can cause severe damage to battery life).

The multifunctional inverter in conjunction with the battery bank allows the PCC's load curve to be regulated, thus relieving the power supplied by the utility and contributing to the voltage levels along the sections of the electricity system, given that the load demand will be supplied locally.

With regard to harmonic compensation, the photovoltaic inverter acts as an active filter, since the harmonic current compensation function was implemented by inserting resonant plots in parallel with the current loop PI controllers. To implement these plots, it was necessary to determine the gain of each resonant controller. This was done in order to achieve the desired frequency response and obtain a good response in the time domain (without large overshoots and fast dynamics). Finally, a reactive power management control was implemented in order to regulate the voltage and correct the power factor of the local load.

The structure of this paper follows the following organization: Section 2 presents a detailed description of the system under analysis, while Section 3 explores the methodology employed for the modeling and control of the system. Section 4 addresses the proposal for the operation of the inverter performing the proposed ancillary services, while the results of the simulations are presented in Section 5. Finally, Section 6 presents the discussion of the results, Section 7 presents the conclusion of the article, as well as proposals for future work and Appendix A presents the values of the parameters used in the algorithms.

2. System under Analysis

Considering that most of the works present renewable generation systems in stable regime and in ideal electrical systems, that is, systems with a high level of short circuit, balanced and without distortion, it is necessary to validate the proposed system in grid that presents behavior like a real grid. In this sense, this section will present the grid model used, as well as the topology of the electronic converter of the renewable generation unit employed.

2.1. Grid Implemented for Interconnection of the Renewable Unit

The grid selected for the computational implementation was the IEEE 13-bus system. This topology was chosen because it is a consolidated grid, with non-ideal characteristics that represent with a degree of accuracy an urban radial distribution grid. For example, it is a highly charged short grid, it has area and underground lines, it has shunt capacitors, it also has an unbalanced charging [27]. In addition, to validate the response of the renewable generating unit to the ancillary frequency support service, a microgrid was implemented which will connect to the IEEE 13-bus system, as shown in Figure 1.

As can be seen in Figure 1, the renewable generation unit was connected in parallel to a synchronous machine of 2 MVA that in turn is responsible for feeding, primarily, the L1 and L2 loads. In addition, distributed generation is responsible for supplying the demand of the L4 and L5 load, and the L5 load is a nonlinear load. Finally, it is worth mentioning that the 680 bus was chosen for the connection of the microgrid (Shaded area), because it is a terminal line bus, so this connection point is more susceptible to variations in the power quality indices, such as voltage sag, undervoltage, unbalance, among others. It is also worth noting that the colored lines represent the phases of the network, being red for phase A, green for B and blue for phase C. Table 1 shows the powers of the L1 to L5 loads, as well as their supply voltage levels.

Table 1. Power and supply voltage of microgrid loads.

Load	Power (kVA)	Voltage (kV)
L1	800 + j0	4.16
L2	800 + j400	4.16
L3	45 + j0	4.16
L4	100 + j85	0.8
L5	77 + j3.5	0.8

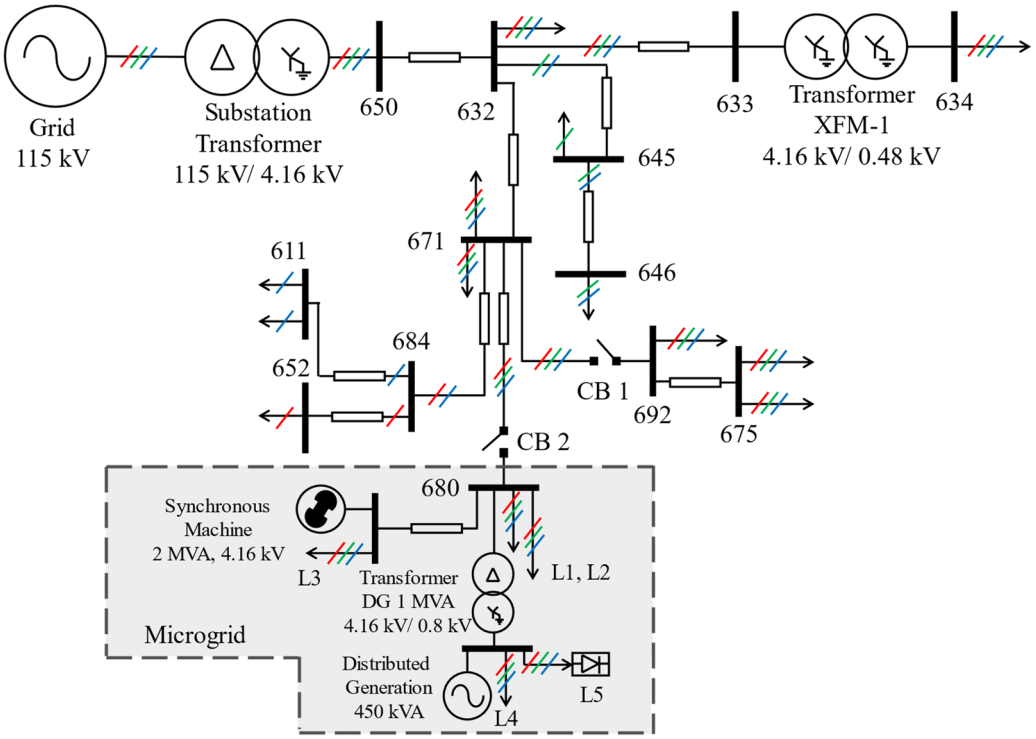


Figure 1. Schematic of the IEEE distribution 13 bus system with microgrid connection.

It is noteworthy that the L4 load is decomposed into five other subloads, as can be seen in Figure 2.

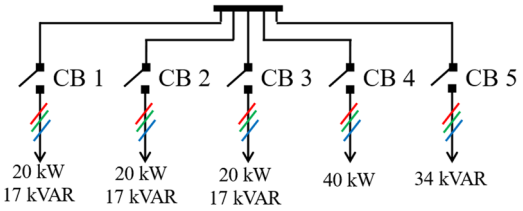


Figure 2. Schematic of the L4 load.

In the analysis of Figure 2 it is verified that the subloads of the L4 load are commanded by power circuit breakers. This topology is used for the validation of the energy management of the energy storage system, which presents the function of smoothing the power demand of the power grid.

2.2. Topology of the Converter of the Renewable Generating Unit

Considering that the photovoltaic generation system, as well as the battery energy storage system operates in direct current and conventional power systems, such as the case of the IEEE 13 bus system, operate in alternating current, it is necessary to use electronic power converters to perform the interfacing of the DC side and the AC side.

In this sense, in this study a two-stage converter topology was used, being the first responsible for managing the photovoltaic generation as well as the storage system. The second stage is intended for power management between the DC side and the AC side. Figure 3 demonstrates a macro view of the system under study.

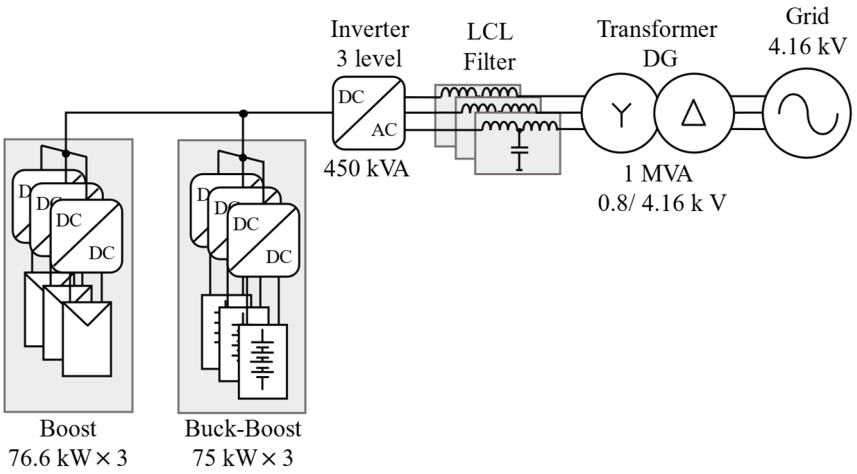


Figure 3. Schematic of the renewable generating unit under study.

According to Figure 3, the topology of the electronic converter is composed of six DC/DC converters, three of which are bidirectional Buck-Boost converters in current responsible for the control of charge and discharge of the battery bank and three are Boost responsible for extracting the maximum power from the photovoltaic arrays. All these systems are interconnected on a DC bus, in addition, each converter has an independent control.

Therefore, the DC bus is interconnected to a three-level NPC (Neutral Point Clamped) inverter. This topology was adopted due to the level of power managed by the generating unit, as well as because it is a widely used topology commercially and in the technical literature [14]. Table 2 shows the operating parameters of the system.

Table 2. Operating parameters of the generating unit.

Parameter	Value	Unit of Measurement
DC/AC converter power (S_{inv})	450	kVA
DC bus voltage (V_{cc})	1500	V
Maximum power of photovoltaic arrays (P_{mpv})	76.6	kW
Voltage at the point of maximum power of the arrangements (V_{mpv})	1346	V
Current at the point of maximum power of the arrangements (I_{mpv})	58.3	A
Open circuit voltage of the arrays (V_{ocpv})	1664	V
Short-circuit current of the arrangements (I_{ccpv})	62	A
Nominal voltage of battery banks (V_{nbat})	1239	V
Rated current of battery banks (I_{bat})	50	A
Battery seat capacity (Q_{bat})	125	Ah
Rated power of battery banks (P_{nbat})	75	kW

3. System Modeling and Control

This section will address the methodologies adopted for the modeling and control of the systems involved in the operation of the renewable generating unit. In this sense, the modeling and control of the system is separated into three major sub steps, which are: modeling and control of the Boost converter, the Buck-Boost converter, and the voltage inverter for connection to the grid. Each sub-step will be covered separately below.

3.1. Modeling and Control of the DC/DC Boost Stage

In the first analysis, for the correct modeling of the system, as well as its control must be verified the topology of the converter and the control systems employed. Thus, Figure 4 shows the topology of the Boost converters in conjunction with their control systems.

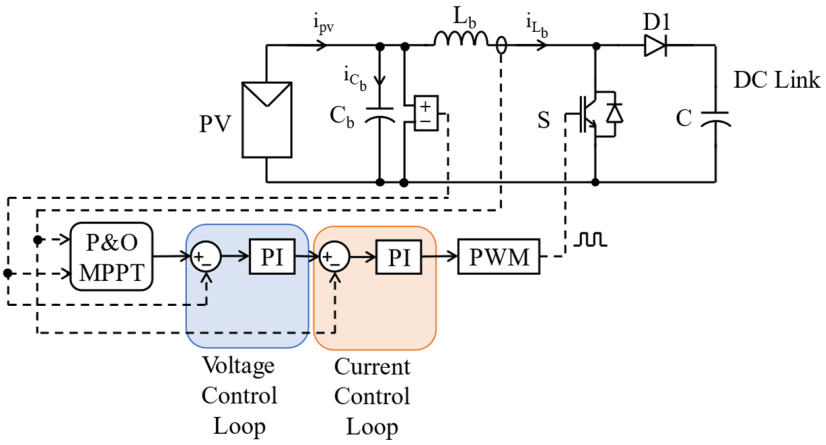


Figure 4. Topology and control loop of Boost converters.

It turns out that the control of the Boost converter is carried out by two cascading loops. The innermost loop is responsible for controlling the current in the converter inductor, while the outermost loop is responsible for controlling the voltage on the input capacitor [28]. Therefore, to perform the voltage reference for the control system, an MPPT P&O algorithm was used, widely used in the technical literature [29]. Therefore, the system in Figure 4 can be represented by a block diagram, shown in Figure 5.

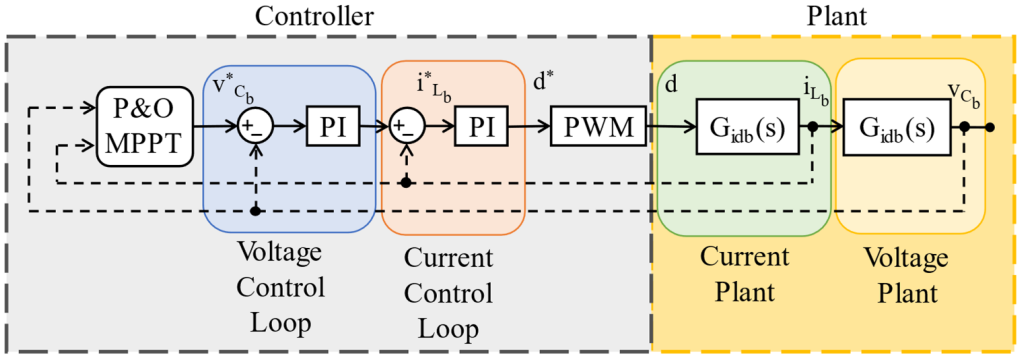


Figure 5. Block diagram for the Boost converter.

The transfer functions $G_{idb}(s)$ and $G_{vib}(s)$ which relate, respectively, the current in the inductor with the work cycle of the S switch and the voltage in the input capacitor with the current in the inductor are obtained by nodal and mesh analysis, applying Kirchhoff's Law of currents and voltages. Thus, for the transfer function $G_{idb}(s)$, applying Kirchhoff's law of currents to the capacitor C_b yields:

$$i_{pv} = i_{C_b} + i_{L_b}$$

$$\frac{V_{pv} - \overline{v_{C_b}}}{R_{eqpv}} = C_b \cdot \frac{d\overline{v_{C_b}}}{dt} + \overline{i_{L_b}} \quad (1)$$

i_{pv} is the current of the photovoltaic array;
i_{C_b} is the input capacitor current of the boost converter;
i_{L_b} is the inductor current of the boost converter;
V_{pv} is the maximum power output voltage of the photovoltaic array;
v_{C_b} is the voltage of the boost converter's input capacitor.
C_b is the capacitance of the boost converter's input capacitor.

In (1) the terms V_{pv} e R_{eqpv} represent the equivalent of Thevenin for the photovoltaic array. This is a simplification adopted in modeling which would assume an equivalent of

the circuit of the photovoltaic array at the point of maximum power. Already the terms highlighted with a slash over the variable ($\overline{x}$), represent mean values of the variables. Subsequently, applying small signs ($\widetilde{x}$) in the terms in the variables of (1) and later applying the Laplace transform, considering only the terms of small signs, the transfer function of interest is obtained.

$$\frac{V_{pv}}{R_{eqpv}} - \frac{\overline{v_{C_b}}}{R_{eqpv}} - \frac{\widetilde{v_{C_b}}}{R_{eqpv}} = C_b \cdot \left(\frac{d\overline{v_{C_b}}}{dt} + \frac{d\widetilde{v_{C_b}}}{dt} \right) + \overline{i_{L_b}} + \widetilde{i_{L_b}}$$

$$-\frac{\widetilde{v_{C_b}}(s)}{R_{eqpv}} = C_b \cdot s \cdot \widetilde{v_{C_b}}(s) + \widetilde{i_{L_b}}(s)$$

$$\frac{\widetilde{v_{C_b}}(s)}{\widetilde{i_{L_b}}(s)} = -\frac{1}{s \cdot C_b + \frac{1}{R_{eqpv}}} = G_{vi}(s) \tag{2}$$

Therefore, by applying Kirchhoff's Law of Voltages to the loop containing the input capacitor, one can determine the transfer function $G_{idb}(s)$. Thus:

$$\overline{v_{C_b}} = \overline{v_{R_{L_b}}} + \overline{v_{L_b}} + \overline{v_S}$$

$$\overline{v_{C_b}} = R_{L_b} \cdot \overline{i_{L_b}} + L_b \cdot \frac{di_{L_b}}{dt} + \overline{v_S}$$

$$\overline{v_{C_b}} = R_{L_b} \cdot \overline{i_{L_b}} + L_b \cdot \frac{di_{L_b}}{dt} + V_{cc} \cdot \left(1 - \overline{d}\right) \tag{3}$$

v_S is the voltage on the IGBT switch;
$v_{R_{L_b}}$ is the voltage of the boost converter's inductor resistor;
V_{cc} is the DC bus capacitor voltage;
R_{L_b} is the resistance of the boost converter inductor;
L_b is the inductance of the boost converter inductor;
d is duty cycle.

Applying small signs (3) and then applying the Laplace transform and disregarding the middle terms, the transfer of interest function is obtained.

$$\overline{v_{C_b}} = R_{L_b} \cdot \left(\overline{i_{L_b}} + \widetilde{i_{L_b}}\right) + L_b \cdot \left(\frac{d\overline{i_{L_b}}}{dt} + \frac{d\widetilde{i_{L_b}}}{dt} \right) + V_{cc} \cdot \left(1 - \overline{d} - \widetilde{d}\right)$$

$$0 = R_{L_b} \cdot \widetilde{i_{L_b}}(s) + s \cdot L_b \cdot \widetilde{i_{L_b}} - V_{cc} \cdot \widetilde{d}(s)$$

$$\frac{\widetilde{i_{L_b}}(s)}{\widetilde{d}(s)} = \frac{V_{cc}}{s \cdot L_b + R_{L_b}} = G_{idb}(s) \tag{4}$$

From the transfer functions of the plants, PI controllers will be applied. The methodology adopted for the calculation of the gains will be the allocation of poles [30], so in relation to the innermost mesh of current one can write:

$$PI(s) \cdot G_{idb}(s) = \frac{kp_{ib}}{s} \cdot \left(s + \frac{ki_{ib}}{kp_{ib}}\right) \cdot \left(\frac{V_{cc}}{L\left(s + \frac{R_{L_b}}{L_b}\right)} \right) \tag{5}$$

Given that the controller's zero must be equal to the plant pole, we obtain:

$$\frac{ki_{ib}}{kp_{ib}} = \frac{R_{L_b}}{L_b} \tag{6}$$

ki_{ib} is the integral gain of the boost converter's current controller;
kp_{ib} is the proportional gain of the boost converter's current controller;
Simplifying (5) through (6) it is possible to obtain the following equation:

$$PI(s) \cdot G_{idb}(s) = \frac{1}{\frac{s \cdot L_b}{kp_{ib} \cdot V_{cc}} + 1} \tag{7}$$

Equation (7) represents a first-order system, whose cutoff frequency ω_{cb} is given by the term: $\frac{s \cdot L_b}{kp_{ib} \cdot V_{cc}}$. Thus, by defining a cutoff frequency it is possible to calculate the gains of the controllers as:

$$kp_{ib} = \frac{\omega_{cb} \cdot L_b}{V_{cc}} \tag{8}$$

$$ki_{ib} = \frac{\omega_{cb} \cdot R_{L_b}}{V_{cc}} \tag{9}$$

ω_{cb} is the cut-off frequency of the boost converter's current loop;
Carrying out a similar analysis for the voltage loop and considering the current loop as unitary gain, we have:

$$kp_{vb} = -\omega_{vb} \cdot C_b \tag{10}$$

$$ki_{vb} = -\frac{\omega_{vb}}{R_{eqpv}} \tag{11}$$

kp_{vb} is the proportional gain of the boost converter's voltage controller;
ki_{vb} is the integral gain of the boost converter's voltage controller;
ω_{vb} is the cut-off frequency of the boost converter's voltage loop.
It is worth highlighting that the consideration that the current loop is taken as a unitary gain arises from the separation of at least a decade from the cutoff frequency of the internal and external loops. Therefore, considering (8) to (11) and the converter parameters shown in Table 3, it is possible to obtain the frequency response of the Boost converter control system, shown in Figure 6.

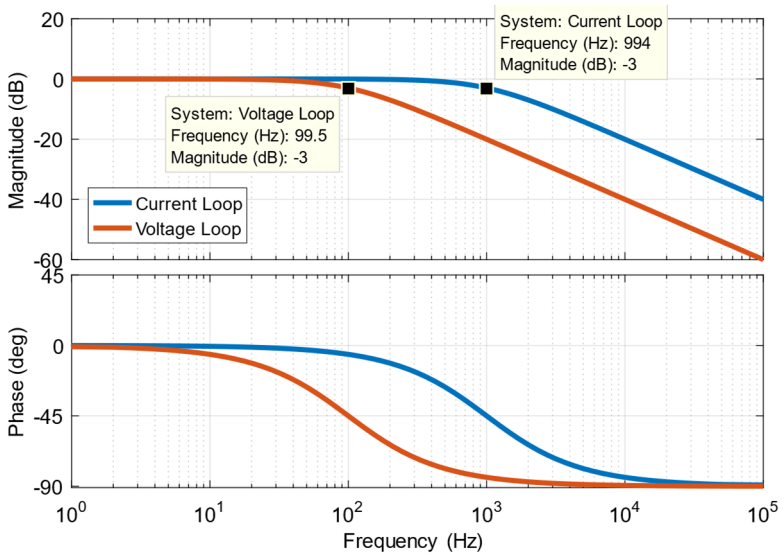


Figure 6. Frequency response of the control loops of the Boost converters.

Table 3. Constructive parameters of Boost converters.

Parameter	Value	Unit of Measurement
Inductance of Boost converters (L_b)	5.5488	mH
Inductor resistance of Boost converters (R_{L_b})	0.1	Ω
Boost input capacitance (C_b)	5.4354	uF
Boost output capacitance (C)	62.5	mF
Equivalent voltage of the photovoltaic array (V_{pv})	1330	V
Equivalent photovoltaic array resistor (R_{eqpv})	22.7195	Ω
Switching frequency (f_{sw})	10	kHz

As can be seen in the frequency response of the system, the cutoff frequency of the current loop has a value ten times lower than the switching frequency [30], this aspect is necessary to consider PWM modulation in modeling as a gain unitary. In turn, the cut-off frequency of the voltage loop has a value ten times lower than the cut-off frequency of the current loop, thus ensuring an adequate distance of one decade from the poles of the control loops [30]. In addition to the frequency response for the correct validation of the gains found, it is necessary to analyze the response in the time domain, which in turn is shown in Figure 7.

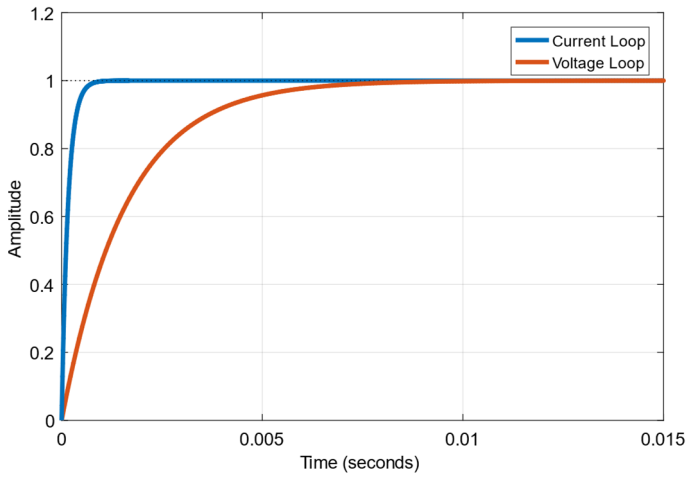


Figure 7. Unit step response of Boost converters control loops.

Observing Figure 7 it is possible to verify that, for both control loops, stable responses were obtained without error in steady state to a current and voltage step. Furthermore, it is possible to see that the settling time for the current loop is ten times shorter than the settling time for the voltage loop, thus reflecting the cutoff frequencies of both loops.

3.2. Modeling and Control of the DC/DC Buck-Boost Stage

The converter topology, as well as the control system used, can be seen in Figure 8.

The converter topology used, as shown in Figure 8, allows power flow in both directions, that is, it allows the battery to be charged and discharged without the bank or DC bus voltages being switched. To control the charging or discharging current, a PI controller is used, which receives the reference from an upstream system responsible for calculating the reference current, allowing the selection of the operating mode and the charging, or discharging power depending on the services. ancillary executed. Each sub-step will be treated separately. The system in Figure 8 can be simplified into a block diagram, as shown in Figure 9.

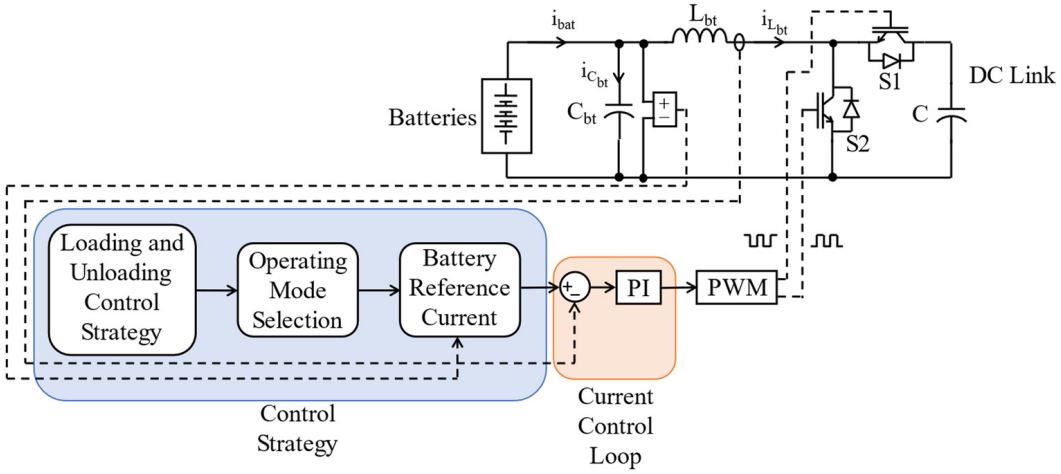


Figure 8. Topology and control loop of Buck-Boost converters.

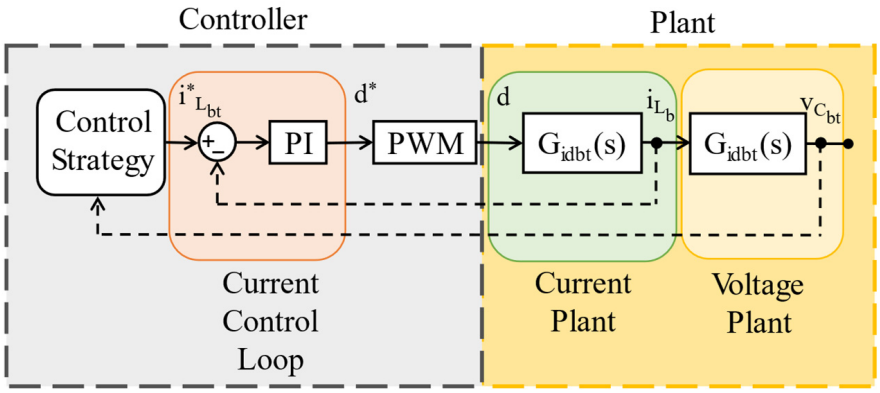


Figure 9. Block diagram for Buck-Boost converter.

As with modeling the Boost converter, it is possible to apply a similar process to the Buck-Boost converter. In this sense, it is worth highlighting that the Thevenin equivalence of the battery bank circuit is performed for the battery to operate in the nominal region, since in this state the battery has little voltage variation for a wide range of charge states, as demonstrated in Figure 10, thus resembling a constant voltage source. The battery model used is the one available in the Simulink software, which is widely used in the technical literature [31,32].

Carrying out the modeling in a similar way to what was previously done for the Boost converter, it is possible to determine the gains of the battery bank current controller, according to (12) and (13).

$$kp_{ibt} = \frac{\omega_{cbt} \cdot L_{bt}}{V_{cc}} \tag{12}$$

$$ki_{ibt} = \frac{\omega_{cbt} \cdot R_{L_{bt}}}{V_{cc}} \tag{13}$$

kp_{ibt} is the proportional gain of the buck-boost converter's current controller;
ki_{ibt} is the integral gain of the buck-boost converter's current controller;
ω_{cbt} is the cut-off frequency of the buck-boost converter's current loop;
$R_{L_{bt}}$ is the resistance of the buck-boost converter inductor;
L_{bt} is the inductance of the buck-boost converter inductor;

For correct operation of the converter, switches S1 and S2 must operate in a complementary manner. Thus, for the converter's construction parameters shown in Table 4, it is possible to evaluate the response in frequency and in the time domain, shown in Figures 11 and 12.

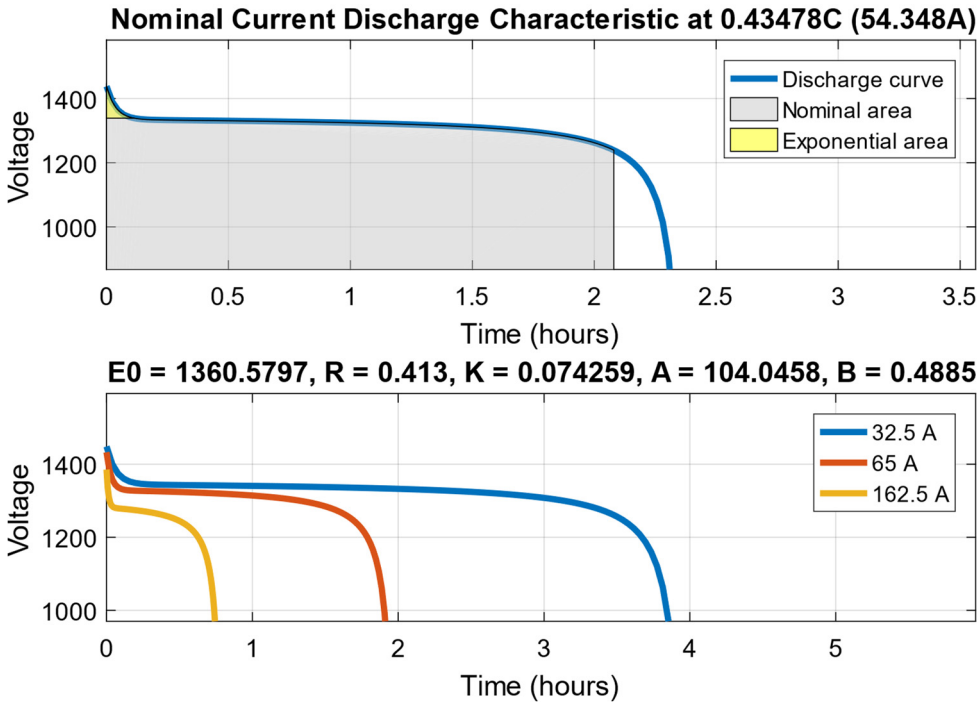


Figure 10. Discharge characteristic curve of the energy storage system.

Table 4. Constructive parameters of Buck-Boost converters.

Parameter	Value	Unit of Measurement
Inductance of Buck-Boost converters (L_{bt})	6.0865	mH
Inductor resistance of Buck-Boost converters ($R_{L_{bt}}$)	0.1	Ω
Buck-Boost input capacitance (C_{bt})	4.7318	uF
Buck-Boost output capacitance (C)	62.5	mF
Battery bank equivalent voltage (V_{bt})	1320	V
Equivalent battery bank resistor (R_{eqbt})	24.2879	Ω
Switching frequency (f_{sw})	10	kHz

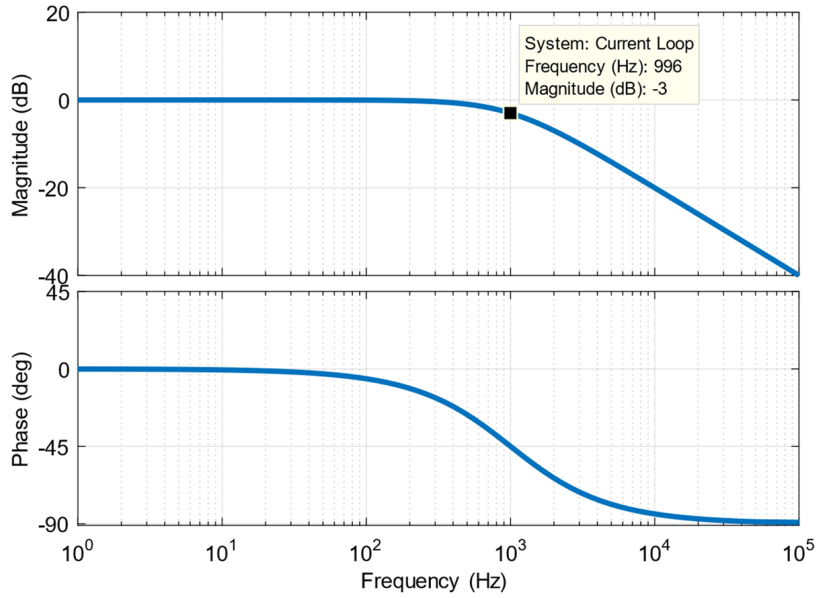


Figure 11. Frequency response of Buck-Boost converter control loops.

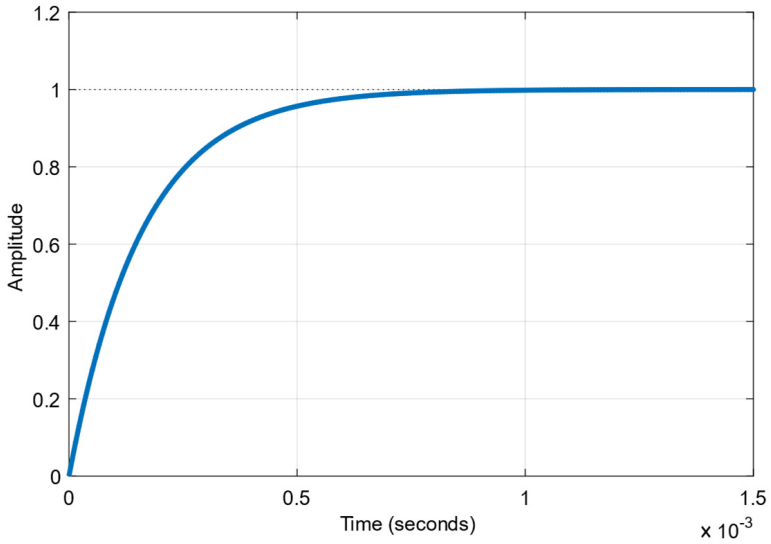


Figure 12. Unit step response of Buck-Boost converter control loops.

Note that the system was designed so that the current control loop has a cut-off frequency at least ten times lower than the switching frequency. Furthermore, when analyzing the response in the time domain, it is verified that the system is stable and does not present an error in steady state.

3.3. DC/AC Stage Modeling and Control

To connect the renewable generating unit to the electrical grid, it is necessary to use an electronic converter to convert the DC level of the DC bus to the AC level. In this sense, a three-level NPC inverter was adopted; the choice of this topology was based on the wide use of this converter in the technical literature [33], as well as because it is widely used in medium and high-power applications [34]. All control was carried out in a synchronous reference, as there is the possibility of using classical linear controllers [35]. The converter topology, as well as the control systems used can be seen in Figure 13.

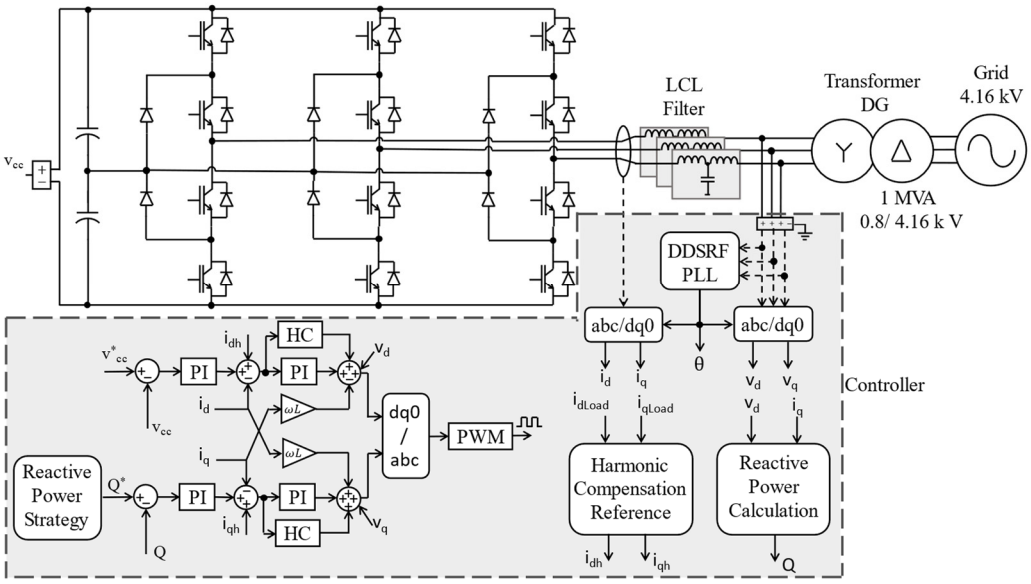


Figure 13. Topology and control loops of the inverter converter.

As shown in Figure 13, the converter current control loop is divided into a direct axis and quadrature mesh, in this sense, there is a more external mesh responsible for controlling

the DC bus voltage (on direct axis) and a mesh responsible for controlling reactive power (in quadrature axis). For reactive power management, a strategy was implemented that will be discussed shortly, as well as harmonic compensation. To synchronize the converter with the grid, DDSRF-PLL was used, implemented according to [36]. Furthermore, an LCL filter was used to attenuate multiple harmonics of the switching frequency, which was implemented according to [37].

Therefore, for modeling the converter, it was considered that the equipment will be connected to a balanced grid without voltage distortions and that the LCL filter has a predominantly inductive resistive behavior, so the following equations are valid in the frequency domain.

$$V_{id} = (sL_f + R_f)I_d(s) + \{V_{rd}(s) - \omega_r L_f I_q(s)\} \quad (14)$$

$$V_{iq} = (sL_f + R_f)I_q(s) + \{V_{rq}(s) + \omega_r L_f I_d(s)\} \quad (15)$$

Thus, from (14) and (15) we have the block diagram seen in Figure 14, which already has the PI controller inserted. It is worth noting that the terms in braces are compensated by a feedforward action. It should also be noted that L_f is the total inductance of the LCL filter, V_{rd} is the direct axis voltage of the grid, V_{rq} is the quadrature axis voltage of the grid, V_{id} is the direct axis voltage synthesized by the inverter, V_{iq} is the voltage quadrature axis synthesized by the inverter, ω_r is the angular frequency of the grid and I_d and I_q are the direct axis and quadrature currents injected by the inverter.

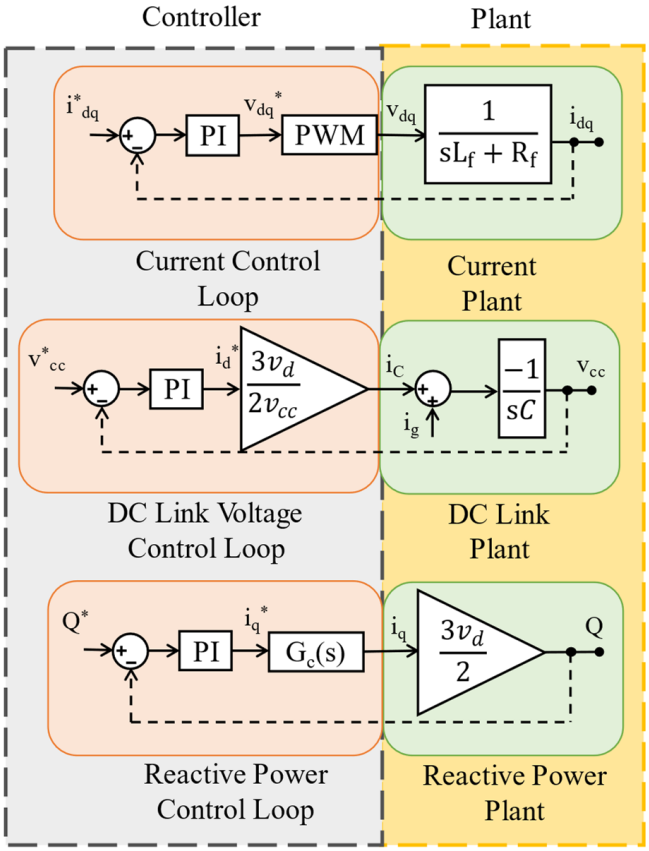


Figure 14. Block diagram for the DC/AC converter.

In a similar way to what was done for DC/DC converters, the gains of the DC/AC converter controllers were found by pole allocation. In this sense, it was established as a design requirement that the cutoff frequency of the current loop must be at least ten times lower than the switching frequency [30], therefore it is possible to simplify the PWM block

by a unity gain. In addition to the direct and quadrature axis current control loops, two external loops were implemented, one for DC bus voltage control and the other for reactive power, respectively in the direct and quadrature axes. The cutoff frequency of these loops was stipulated as being at least ten times lower than the cutoff frequency of the current control loops [30].

Thus, using the data in Table 5 it is possible to calculate the controller gains and obtain the frequency and time domain responses of the systems. This data can be viewed in Figures 15 and 16.

Table 5. Constructive parameters of the inverter.

Parameter	Value	Unit of Measurement
Inductance converter side of LCL filter (L_1)	0.5443	mH
LCL filter net side inductance (L_2)	0.0574	mH
Total resistance of the LCL filter (R_f)	30	mΩ
DC bus capacitance (C)	62.5	mF
DC bus voltage (V_{cc})	1500	V
Switching frequency (f_{sw})	10	kHz

Analyzing the frequency response of the system, the distance between the cutoff frequencies of the meshes in question is observed, therefore meeting the design criteria. Therefore, checking the response in the system's time domain, the system is stable and has zero error in steady state. It can also be noted that the mesh settling time is within the acceptable range to ensure proper operation of the converter.

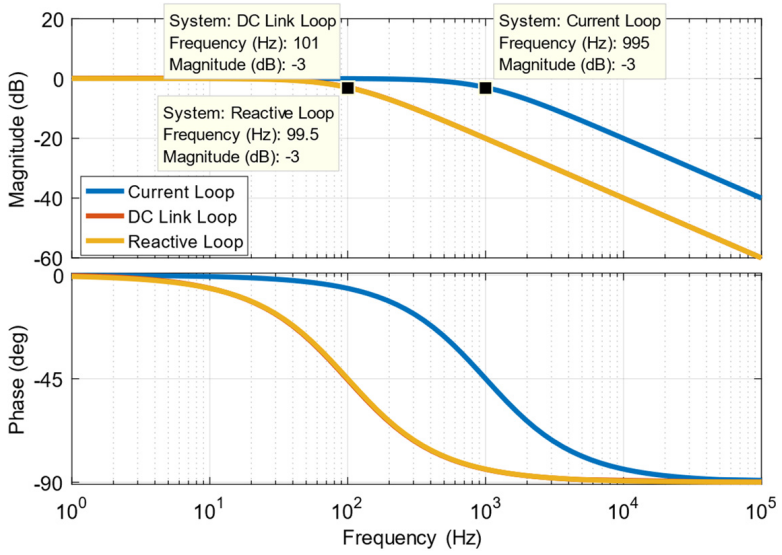


Figure 15. Frequency response of the DC/AC converter control loops.

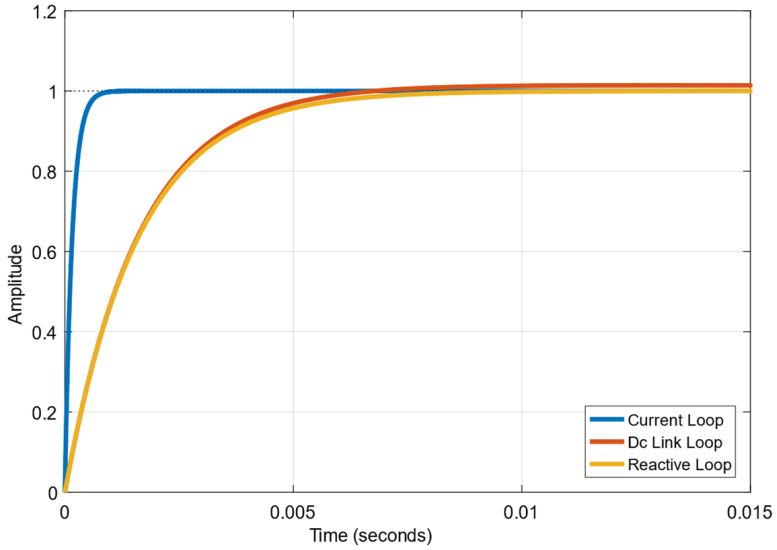


Figure 16. Response to the unit step of the control loops of the DC/AC converter.

4. Proposal for Inverter Operation Performing Ancillary Services

In this section, the operation of the DC/AC converter will be discussed, performing the ancillary services of frequency support, voltage support, active power dispatch and load curve regulation and harmonic current compensation at the point of common coupling (PCC). Each function will be covered separately.

4.1. Frequency Support

The frequency support implemented in this work will be based on the absorption or supply of active power to the PCC. This characteristic assumes that the electrical power supplied by a conventional synchronous machine is predominantly related to the energy that is supplied to that machine by the primary motor [25]. In this sense, for the frequency support was implemented a control system of the type droop $P - f$, given by (16), where R_F is the statism of the droop control in steady state.

$$\Delta P = \Delta f \cdot R_F \tag{16}$$

ΔP is the variation in active power injected by the generating unit;
Δf is the frequency variation of the network;
R_F is the steady-state frequency.

Equation (16) suggests that the variation in active power caused by the converter depends exclusively on the gain associated with static, as well as the amplitude of variation in grid frequency, thus being directly proportional to these quantities. However, it is necessary to implement power saturators, so that the power limits of the converters are not exceeded. In this sense, droop control with upper and lower saturator was implemented, which has the characteristic curve shown in Figure 17.

From Figure 17, as the system frequency decreases, more active power is supplied, while as the system frequency increases, more active power is absorbed from the grid. This behavior is not possible to be implemented in most synchronous machines that operate as generators, as the prime mover generally does not accept a reverse power flow. The limits of absorbed and supplied power are determined depending on the powers of the DC/AC and DC/DC converters, the latter being responsible for absorbing or supplying active power, while the former acts as an intermediary in the exchange of energy between the grid and the bus DC.

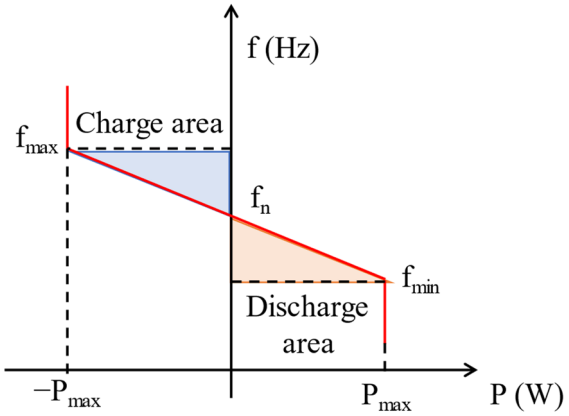


Figure 17. Droop feature for frequency support.

4.2. Reactive Power Support

Like what was performed for the frequency support, the reactive power support also uses the strategy of droop control, however relating Q − V, as is commonly performed for traditional synchronous machines [38]. The equation that governs this control is evidenced in (17).

$$\Delta Q = \Delta V \cdot R_V \quad (17)$$

ΔQ is the variation in reactive power injected by the generating unit;
ΔV is the mains voltage variation;
R_V is the steady-state voltage.

Therefore, when significant voltage variations occur in the PCC, substantial variations in reactive power also occur, as well as the higher the droop constant, the greater its sensitivity to voltage variations. Figure 18 shows the characteristic curve of this control.

In analyzing Figure 18, the converter has the possibility of operating inductively or capacitively, seen from the grid. When there is a positive voltage variation in the grid, its behavior resembles that of an inductive load, absorbing reactive power from the PCC, consequently tending to reduce the voltage at this point. On the other hand, when there is a negative voltage variation, the converter behaves as a capacitive load for the system, injecting reactive and, consequently, tending to increase the voltage at the PCC.

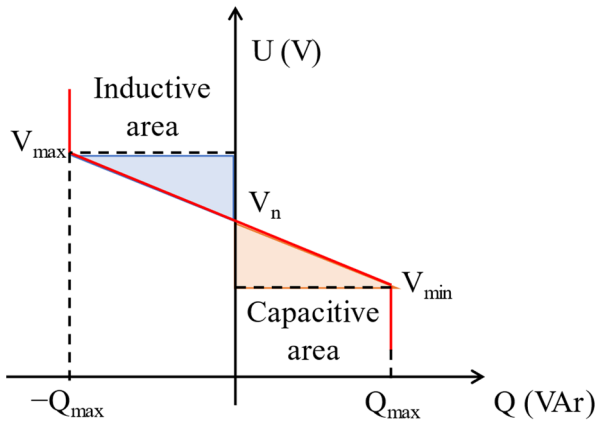


Figure 18. Droop feature for reactive power support.

Occasionally, reactive power may be requested from the converter in such a way that, in its current situation (injecting or consuming active power from the PAC), if this demand is met, its nominal apparent power limit will be exceeded, consequently the current limit of the DC/AC converter switches has been violated. For this to be avoided, an algorithm was implemented that will act on the storage system so that a power margin from the DC/AC

converter is generated and consequently the reactive power demand is met. Figure 19 demonstrates the inverter capability curve, which will be used to explain the algorithm.

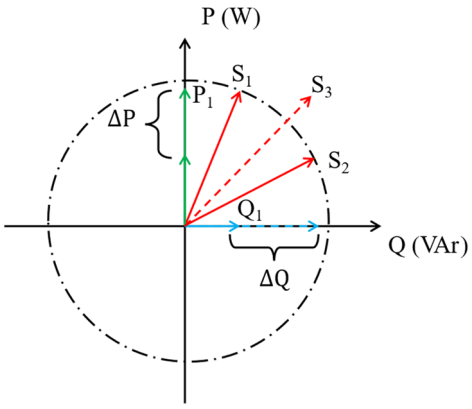


Figure 19. Operation of the DC/AC converter according to its capability curve.

From Figure 19, the inverter operated by injecting a power P_1 and Q_1 into the grid, consequently, it operated with a nominal apparent power S_1, such that:

$$S_1 = \sqrt{P_1^2 + Q_1^2} \tag{18}$$

At a certain point there was a greater demand for reactive power represented by a variation ΔQ, so if the inverter met this demand and continued injecting the active power P_1 its new apparent power would be S_3, thus exceeding its nominal limits. Thus, for the reactive demand to be met, it is necessary to decrease the injected active power represented by the variation ΔP, so that the converter returns to its nominal limits operating with an apparent power S_2, therefore:

$$S_1 = S_2 = \sqrt{P_1^2 + Q_1^2} = \sqrt{(P1 - \Delta P)^2 + (Q1 + \Delta Q)^2} \tag{19}$$

Therefore, in order to reduce active power in the DC/AC converter and to avoid the need to reduce photovoltaic generation, the power difference ΔP can be redirected to the battery bank, if it has the capacity to drain such power, as demonstrated in Figure 20.

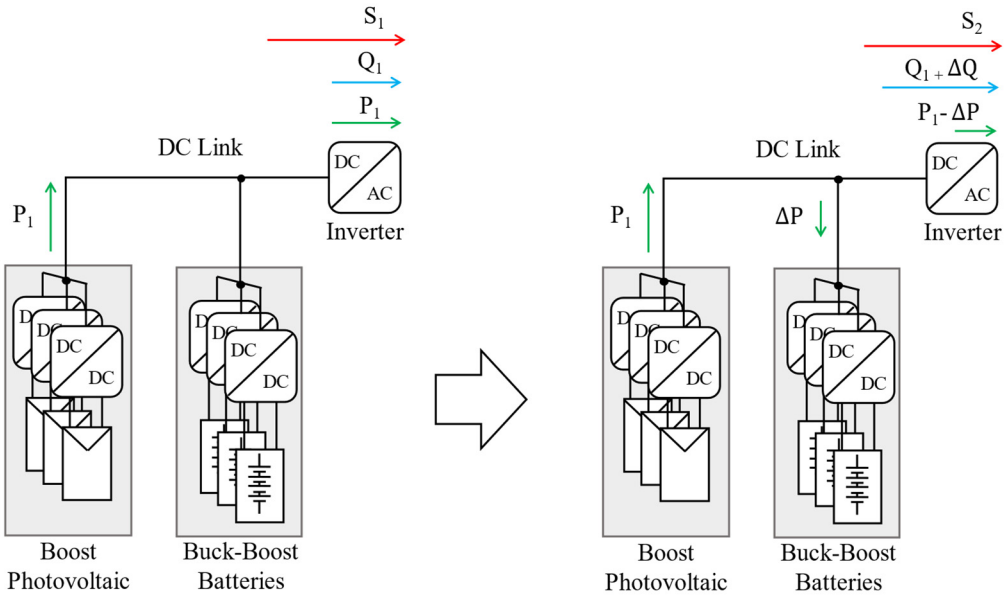


Figure 20. Power flow in the generating unit during active power relief.

It is evident in Figure 20 that after the algorithm has been activated, the difference in active power is allocated to the storage system. In (20) the equation for obtaining the reference power P_{ref} that must be absorbed by the storage system is demonstrated, where P_{pv} is the power from photovoltaic generation, S_n is the nominal power of the DC/AC converter and Q_{ref} is the power reference reactive.

$$P_{ref} = P_{pv} - \sqrt{S_n^2 - Q_{ref}^2} \tag{20}$$

Thus, the reactive power strategy block shown in Figure 13 can be seen in Figure 21.

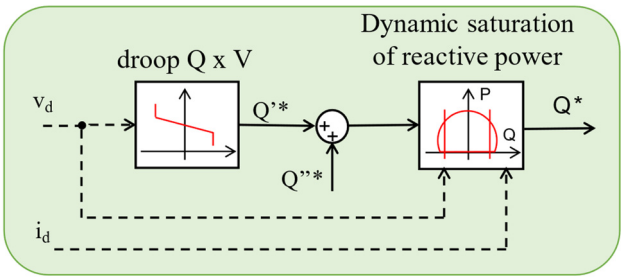


Figure 21. Reactive power management strategy.

In Figure 21, the reactive power reference is generated through the $Q - V$ droop control and an additional input, which can come from an external controller, for example. These power references are added together and saturated by a dynamic reactive power saturator, which aims to guarantee the operation of the DC/AC converter within its nominal apparent power limits. The upper Q_{up} and lower Q_{dw} saturation reactive power values are obtained by (21) and (22), respectively.

$$Q_{up} = \sqrt{S_n^2 - \left(\frac{3}{2} V_{rd} \cdot I_d\right)^2} \tag{21}$$

$$Q_{dw} = -\sqrt{S_n^2 - \left(\frac{3}{2} V_{rd} \cdot I_d\right)^2} \tag{22}$$

4.3. Active Power Dispatch and PCC Load Curve Regulation

In relation to the active power dispatch, the power reference to be dispatched must be added to the power reference coming from the droop control $P - f$. This external reference can come from an external controller or can be implemented internally in the converter.

Regarding the regulation of the load curve of the PCC, the reference power to be compensated is obtained by (23) and (24), where P_{disc} and P_{charg} are the unloading and charging powers respectively, $P_{load_{L4}}$ is the power of the L4 load, $P_{load_{L5}}$ is the power of the L5 load, $P_{load_{L3}}$ is the potentiated L3 charge and P_{pv} is the power of photovoltaic generation.

$$P_{disc} = \left(P_{load_{L4}} + P_{load_{L5}}\right) - \left(P_{pv} - P_{loadL3}\right) \tag{23}$$

$$P_{charg} = \left(P_{pv} - P_{loadL3}\right) - \left(P_{load_{L4}} + P_{load_{L5}}\right) \tag{24}$$

In analyzing (23) and (24) it is possible to conclude that the power to be compensated, in a generalized way, is the result of the difference between the load power and the photovoltaic generation power. For this compensation to be adequate, the energy storage system, photovoltaic generation, and the loads must be compatible in terms of power. Furthermore, this compensation must not be performed simultaneously with the frequency support ancillary service, so the frequency condition of the grid must be constantly evaluated.

Finally, the execution of ancillary services of frequency support, active power dispatch and load curve regulation must be performed only when the energy storage system has the capacity to absorb or supply power. In this sense, an algorithm was implemented that evaluates the reference power of the storage system and determines whether this power can be delivered, as shown in Figure 22. It is worth mentioning that the SOC refers to the state of charge of the batteries and the ω the angular frequency of the grid.

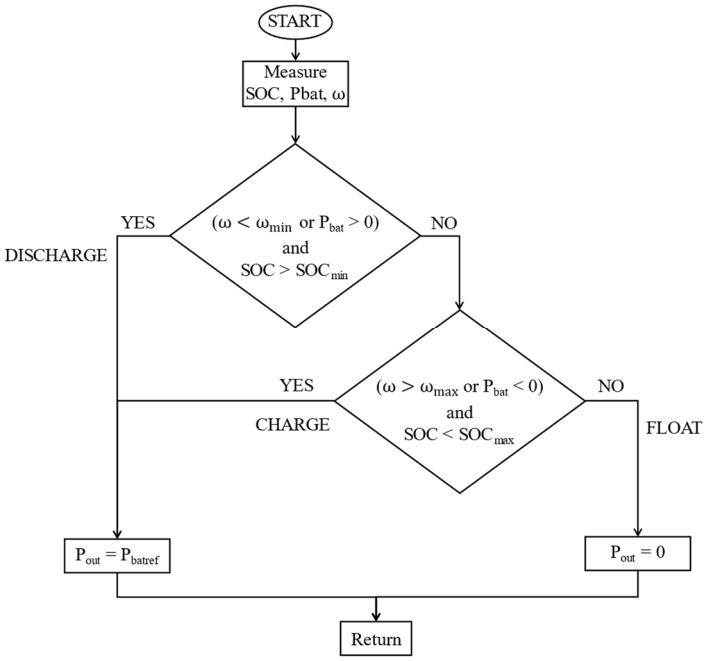


Figure 22. Algorithm for active potency relief.

As demonstrated in the algorithm in Figure 22, the output power (P_{out}) will be equal to the reference (P_{batref}) provided that the power sense conditions are met in conjunction with frequency variations (ω) and battery state of charge (SOC). Thus, the control strategy of the energy storage system demonstrated in Figure 8 can be represented by the control loop in Figure 23.

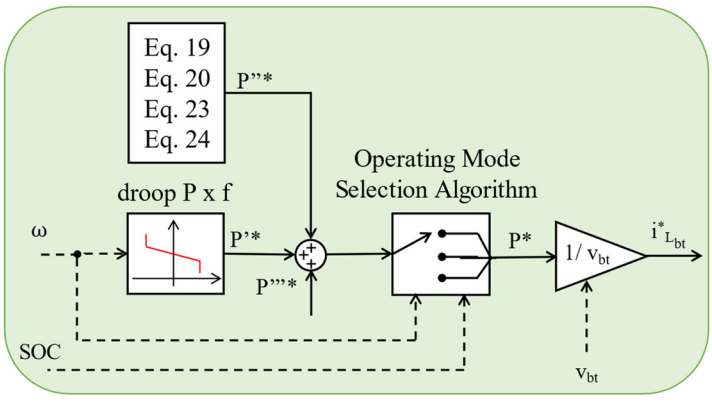


Figure 23. Energy storage system control strategy.

Figure 23 shows the control strategy loop of the energy storage system. It consists of the P x f droop control, the references from the active power relief (P''^*), the load curve management system (P''^*), the battery operating mode selection algorithm, an external power reference (P'''^*) and the calculation of the storage system current ($1/V_{bt}$). The current is calculated from the reference power (P^*) and the battery bank voltage.

4.4. Harmonic Current Compensation

Harmonic current compensation is carried out using PI controllers with resonant plots, as implemented in [35,39]. The resonant portions are determined by (25). Where K_{ih} is the gain for the resonant portion, ω_c is the frequency margin of the resonant portion and h is the harmonic order to be compensated in synchronous reference.

$$HC(s) = \frac{2 \cdot K_{ih} \cdot \omega_c \cdot s}{s^2 + 2 \cdot \omega_c \cdot s + (h \cdot \omega)^2} \quad (25)$$

In this work, three resonant plots were used, which were parameterized for 6th, 12th and 18th order harmonics, which represent 5th, 7th, 11th, 12th, 13th, 17th and 19th order harmonics. It should be noted that the fundamental frequency is given as 60 Hz. Figure 24 shows the frequency response of the system containing the resonant portions.

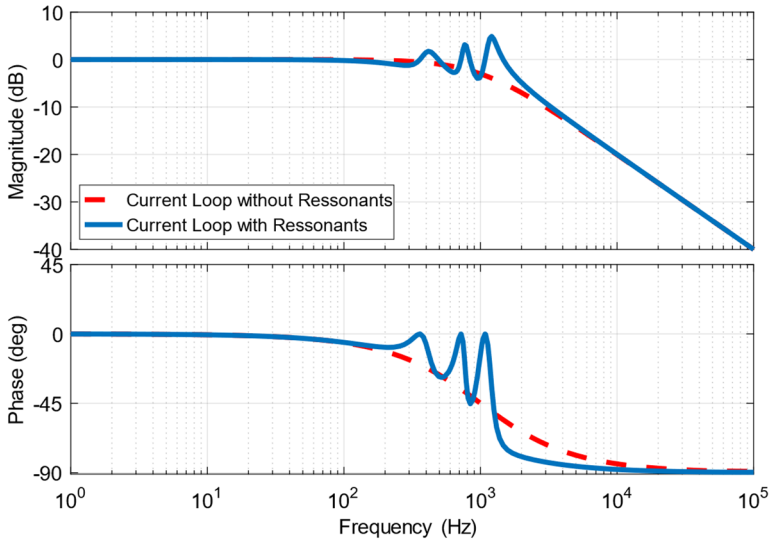


Figure 24. Frequency response of the inverter current control loop with resonant portions.

As shown in Figure 24, the resonance peaks occur at the aforementioned frequencies in synchronous reference. Therefore, the phase and magnitude values are taken to unity. Table 6 shows the magnitude and phase values for the system with and without the resonant portions.

Table 6. Magnitude and phase values for the system with and without resonant parcels.

Frequency (Hz)	System without Resonant Parcels		System with Resonant Parcels	
	Magnitude (dB)	Phase (°)	Magnitude (dB)	Phase (°)
360	−0.529	−19.8	−0.0167	−0.0456
720	−1.83	−35.8	−0.00754	−0.086
1080	−3.34	−47.1	−0.216	−0.12

An analysis of Table 6 shows that as the harmonic order increases, the higher the gain of the resonant section will have to be in order for there to be magnitude and phase correction; consequently, increasing this gain makes the system more oscillatory, reaching high values of current overshoot in the time-domain response. In this sense, the gain and frequency margin of each part were chosen to provide a good frequency response (lower magnitude and phase errors) and also a good time domain response (overshoot limited to 120%). It is worth noting that the phase and frequency compensations were met at the chosen frequencies. Figure 25 shows the response of this system in the time domain.

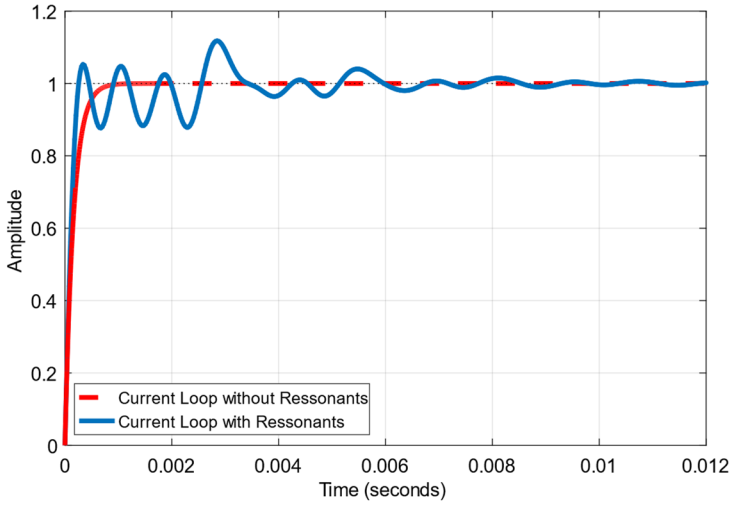


Figure 25. Unit step response of inverter control loops with resonant plots.

Figure 25 shows that the maximum overshoot was 112%, thus meeting the design requirements. Finally, in order to compensate for the harmonic current references, the following strategy was used, as shown in Figure 26.

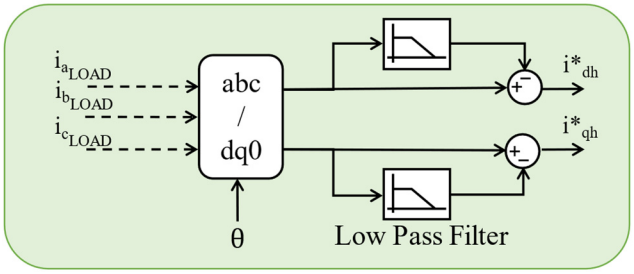


Figure 26. System for generating harmonic current references to be compensated.

As shown in Figure 26, the current reference to be compensated is generated using the reference transform in conjunction with low-pass filters, where θ is the phase angle of the mains voltage. The filter is responsible for extracting the continuous component of the signal (referring to the fundamental frequency), then this signal is subtracted from the original signal, leaving only the oscillating portion, referring to the multiple harmonics of the grid fundamental frequency.

5. Results

This section shows the results of the computer simulations carried out. Therefore, this section will be subdivided to deal with the results separately. The results obtained for the ancillary services of frequency support, reactive power support, active power dispatch and regulation of the PCC load curve and compensation of harmonic currents in the PCC will be discussed, all under the influence of the proposed load and discharge control.

5.1. Frequency Support

In order to validate the performance of the frequency support ancillary service, simulations were carried out in which the microgrid is isolated from the main grid and after the circuit is disconnected by means of the CB2 circuit breaker shown in Figure 1, there is a change in photovoltaic generation. Cases were analyzed in which there is a loss or increase in photovoltaic generation and its respective impact on the rotational speed of the synchronous machine with the system operating with and without the battery energy storage system.

In this sense, out of a total simulation period of 4.5 s, at 1 s the microgrid is isolated and at 2.5 s the photovoltaic generation varies for the cases under analysis. Figure 27 shows the frequency variation of the microgrid in the event of a 100% loss of photovoltaic generation and Figure 28 shows the frequency of the microgrid in the event of a 100% increase in the total generation of the photovoltaic generating unit.

As can be seen in Figures 27 and 28, in cases where the generating unit does not have an energy storage system, when there is a variation in generation, there is a frequency variation with high amplitude and oscillation. In cases where the generating unit is equipped with a storage system, the frequency variation amplitudes are attenuated and the oscillations are damped. The response of the system in question is equivalent to that of a system with a greater inertia than the original system. This characteristic is accentuated by increasing the steady-state (R_F) of the photovoltaic generating unit.

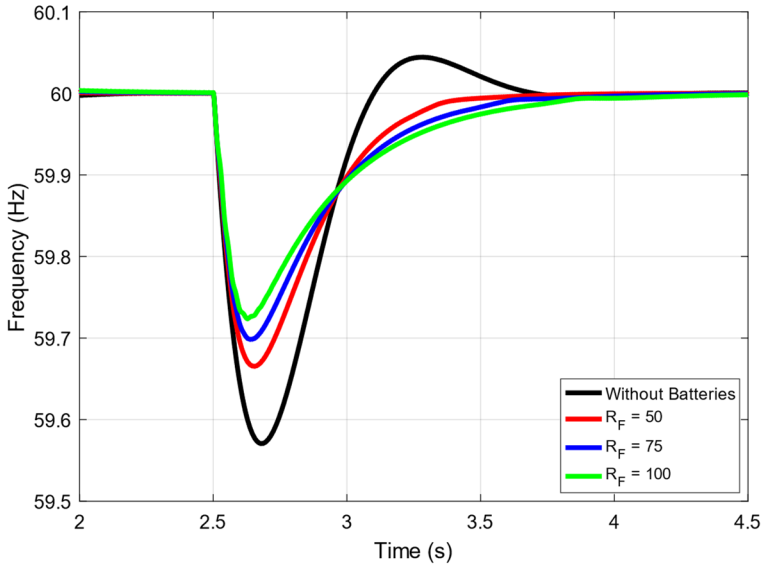


Figure 27. Frequency variation for total loss of photovoltaic generation.

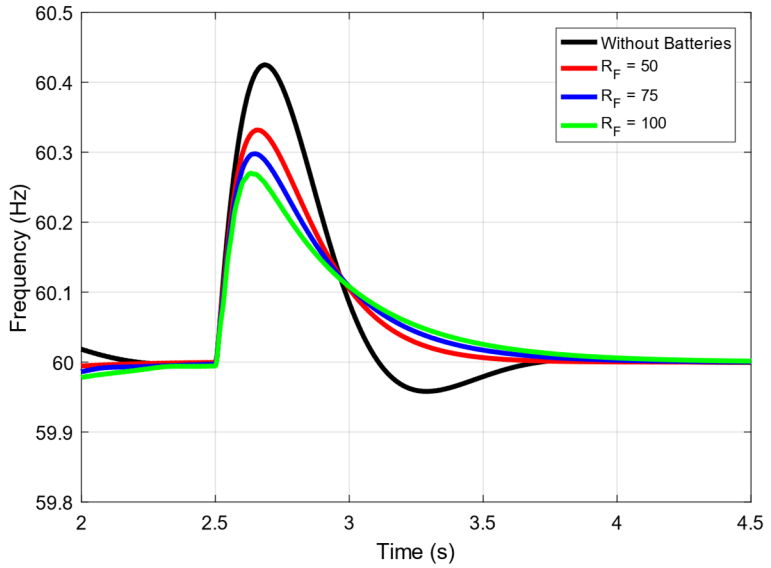


Figure 28. Frequency variation for total increase in photovoltaic generation.

The attenuation of the amplitudes and the damping of the oscillations are due to the action of the storage system. Figures 29 and 30 therefore show the powers flowing through

the storage system and the DC/AC converter of the generating unit during a disturbance in the load-generation balance.

As can be seen in Figures 29 and 30, when a disturbance occurs, the energy storage system responds by supplying or absorbing power to re-establish the load-generation balance. It is worth noting that the response to the disturbance is directly related to the droop selected, as well as the dynamic response of the PLL algorithm used and the controllers of the DC/DC Buck-Boost and DC/AC converters. In cases of maximum droop, there is an oscillation in power caused by the frequency oscillation coming from the PLL. However, in general, when the energy storage system is used, the power oscillations from photovoltaic generation become less severe, thus providing greater stability in the face of random oscillations in photovoltaic generation.

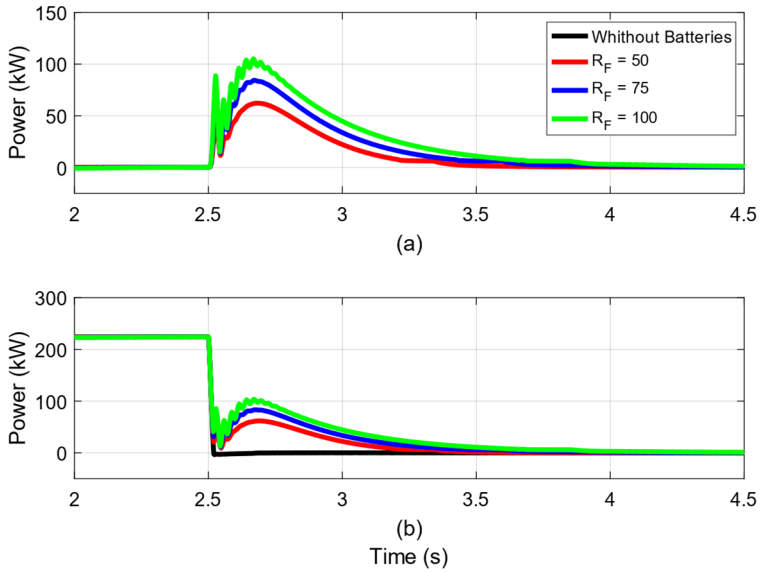


Figure 29. (**a**) Power variation in the storage system during loss of generation; (**b**) Power variation in the DC/AC converter during loss of generation.

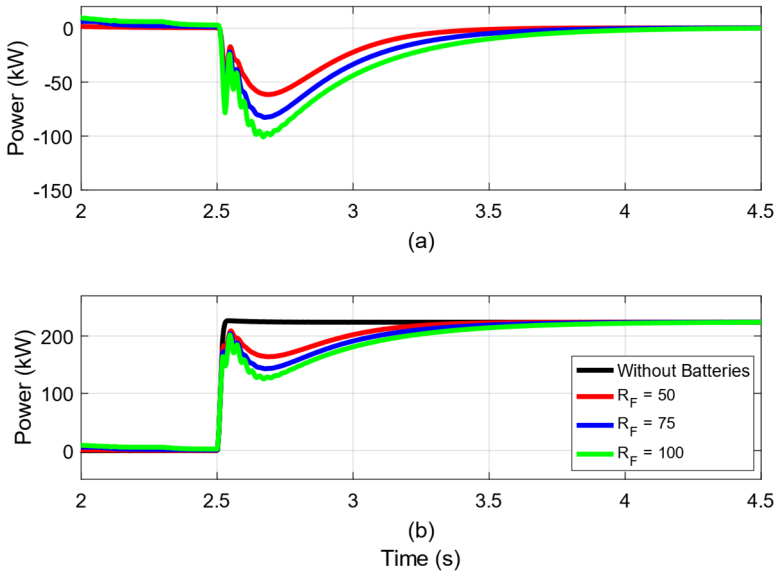


Figure 30. (**a**) Power variation in the storage system during generation input, (**b**) Power variation in the DC/AC converter during generation input.

5.2. Reactive Power Support

The evaluation of the ancillary service of reactive power support was verified with a scenario in which the generating unit dispatched a defined amount of active power, consequently, there was a voltage variation in the PCC of the generating unit and the reactive power control was sensitized.

A 17-s computer simulation was carried out. At the 0.5 s mark, the CB1 circuit breaker and the reactive power support control were triggered, resulting in a voltage drop in the PCC (due to the load coming in through the CB1 circuit breaker) of the generating unit, which led to the reactive power support control being excited. In the following period, up to the instant of 8 s, the renewable unit dispatches active power, thus varying the voltage positively at the PCC. From 9 s to 16 s, the storage system consumed active power, thus characterizing a voltage drop at the PCC. Finally, at 16.5 s the CB1 circuit breaker was opened, thus increasing the voltage at the PCC. The reactive power dispatch is shown in Figure 31.

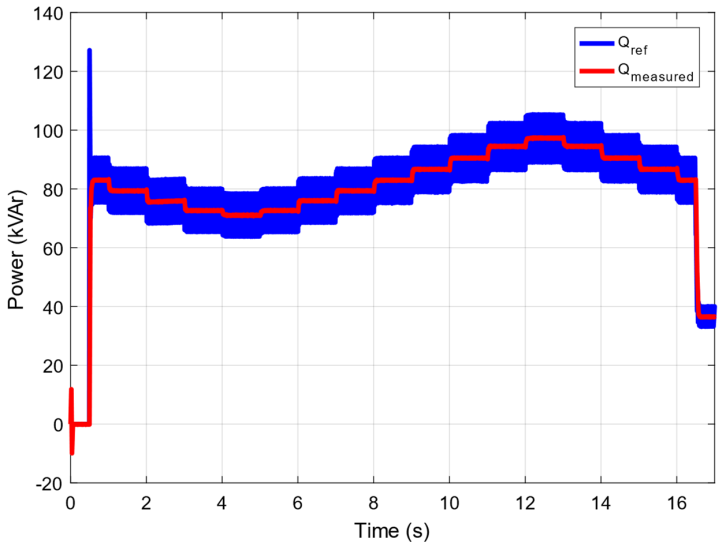


Figure 31. Variation in reactive power dispatched for the reactive power support ancillary service.

Looking at Figure 31, it can be seen that the dispatch of reactive power followed the variation in voltage, which consequently followed the variation in load on the grid. For the reactive power dispatch, a steady-state voltage droop (R_V) of 20 was used.

For this ancillary service, the renewable unit's ability to dispatch a greater amount of reactive power to the detriment of active power dispatch was also assessed. A 4-s simulation was carried out in which the generating unit operated with maximum generation and zero reactive power dispatch. At the 1-s mark, a maximum reactive power dispatch step (450 kVAr) was requested, as shown in Figure 32a. At this point, if the conditions of the algorithm shown in Figure 22 were met, all the photovoltaic generation power was directed to the storage system, as can be seen in Figure 32c, so the generating unit stopped dispatching active power, as shown in Figure 32b. It is worth noting that the power peak at the start of the simulation in Figure 32c is an initialization transient.

In order to assess the impact of reactive power dispatch on the grid voltage, the voltages of phases A, B and C were measured at bar 680, and it was found that when reactive power was dispatched there was an increase in the voltages of the three phases, as shown in Figure 33.

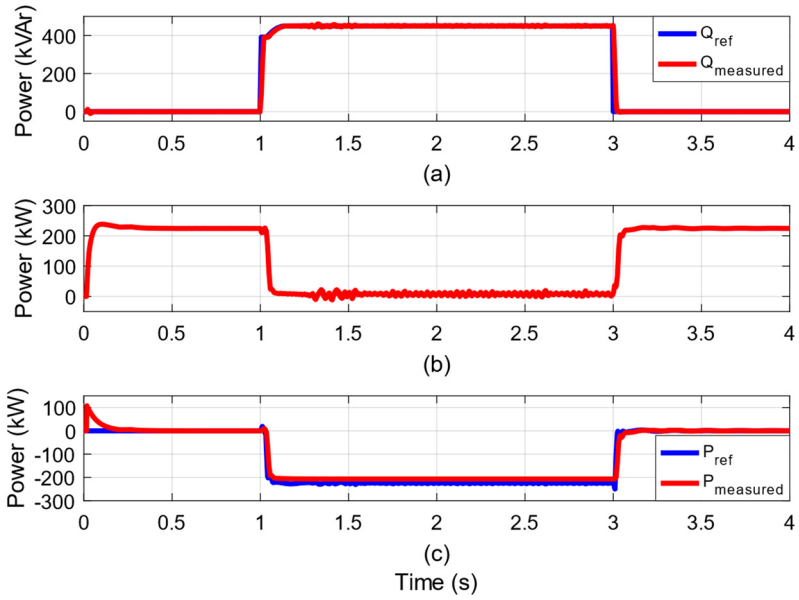


Figure 32. (**a**) Reference reactive power to be dispatched, (**b**) active power dispatched at the PCC, (**c**) power over the energy storage system.

With the dispatch of reactive power, a voltage increase in the three phases of the grid of approximately 1% was observed. This relatively low value is due to the high short-circuit level of the bar in relation to the renewable unit, so if the number of renewable units or the power of the generating unit were increased, greater variations would be observed. It is worth noting that the voltages are slightly unbalanced, which is characteristic of the grid under study.

Based on the performance of the ancillary service of reactive power support, it can be seen that the proposed control increases the efficiency of the energy grid, since there will be an attenuation of the flow of reactive power in the main branches, making it more available to transport active power. Furthermore, in situations where the system has a demand for large amounts of reactive power in relation to the demand for active power, the option can be taken to dispatch this amount of reactive power, but without any loss of generation, since the energy generated by the photovoltaic system will be stored in the battery system, as long as it is available to drain this energy.

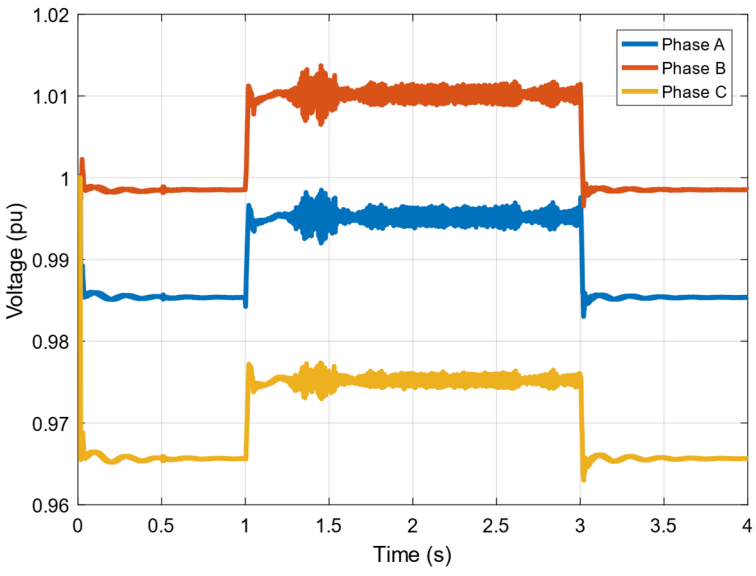


Figure 33. Voltages in phases of bar 680 during reactive power dispatch.

5.3. Active Power Dispatch and Regulation of the PCC Load Curve

The active power dispatch was validated based on the supply and absorption of active power by the energy storage system. To this end, the active power reference shown in blue in Figure 34b was used. This power reference was chosen because it travels between the limits of the energy storage system, and there is also a 1-s period for assessing the stability of the control system. The results obtained are shown in Figure 34.

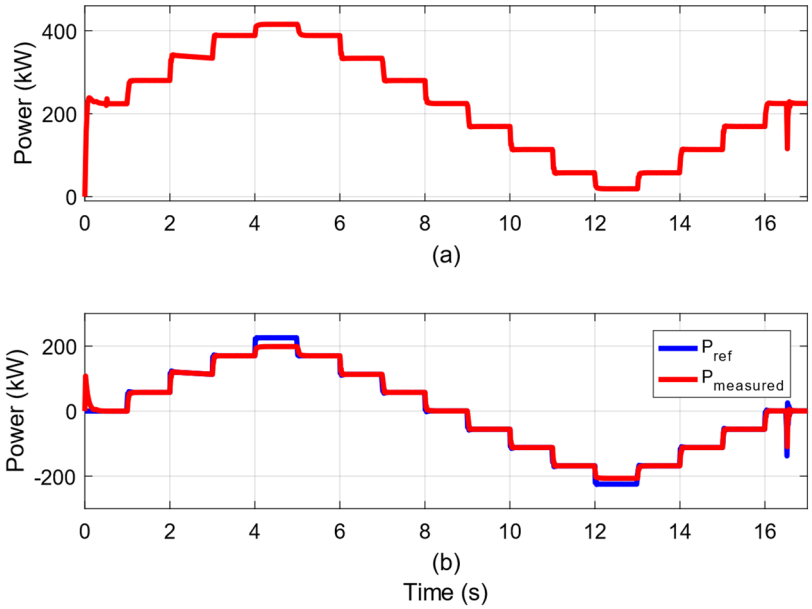


Figure 34. Controlled dispatch of active power by the renewable unit.

According to the data in Figure 34b, it can be seen that the storage system followed the power demand reference, except at the maximum limits, where power was limited by the battery bank's maximum current limit. As the power demand moves towards positive values, the power injected into the grid increases, as shown in Figure 34a, while for negative demand values, the power injected into the grid decreases. It is worth noting that these results were obtained for photovoltaic generation under nominal conditions, that is, irradiance at 1000 W/m^2 and temperature at 25 °C.

The active power dispatch shown can be used to mitigate the grid demand for power at peak times. The storage system can also be charged at times when grid use is low. This strategy ultimately increases efficiency and optimizes the energy system in question.

With regard to the regulation of the PCC load curve, the results obtained are shown in Figure 35.

To obtain the results for the regulation of the PCC load curve, the underloads in Figure 2 were switched via the respective circuit breakers. It is worth remembering that there is a period of 1 s to evaluate the system's response, thus proving its stability. At 2 s the CB1 circuit breaker was switched on, then at 3 s the CB2 circuit breaker was closed, followed by the CB4 circuit breaker at 4 s, then the CB3 circuit breaker was switched on at 5 s, and finally the CB5 circuit breaker at 6 s. The activation of these respective loads demands active and reactive power from the PCC, represented by the red and blue dotted curves, respectively. In addition, the influence of the photovoltaic unit with and without the storage system was verified, whose generated power varied from the nominal value of approximately 10% of this respective value, between the period of 3 and 5 s.

Looking at Figure 35, it can be seen that the power demand curve at the PCC for the case in which the conventional photovoltaic unit is connected suffers abrupt variations in reactive power (black curve) and especially active power (green curve). In certain scenarios, this variation can overload the grid to which the DG is connected, and in some cases, it can lead to frequency or voltage instability [40,41]. In cases where DG with ancillary services

is connected, it can be seen that even with abrupt variations in load power, the power demanded from the grid remains constant, thus leading to greater system stability in terms of voltage and frequency.

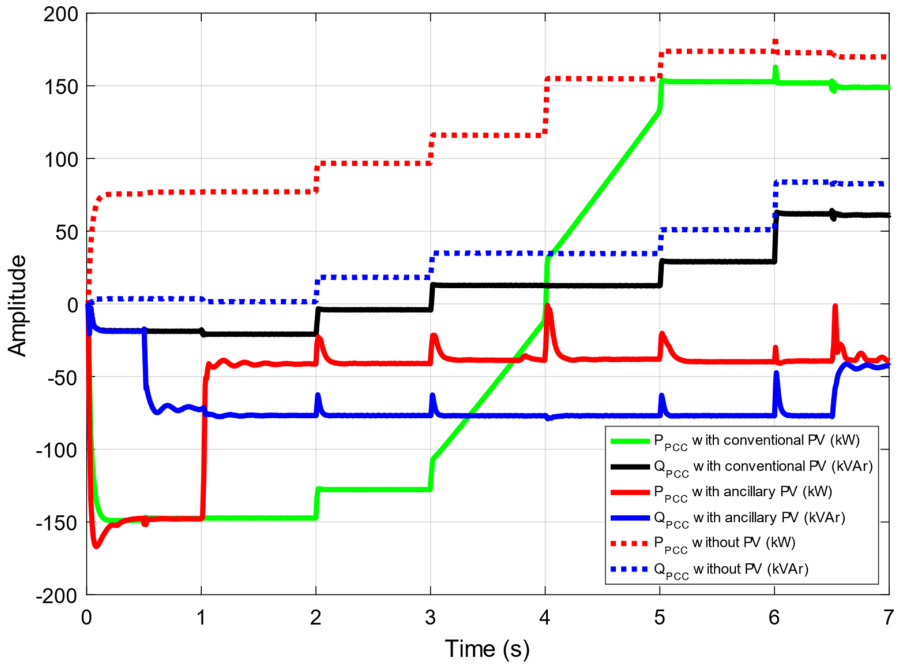


Figure 35. PCC load curves of the system under analysis.

5.4. Compensation of Harmonic Currents in the PCC

To validate harmonic current compensation, a harmonic phonon was used, consisting of a three-phase 6-pulse diode rectifier feeding an RL load (R = 15 Ω and L = 0.1 H). The capabilities of the renewable harmonic compensation unit were evaluated at low levels of dispatched power and at nominal power values. The appearance of the measured currents of interest is shown in Figure 36.

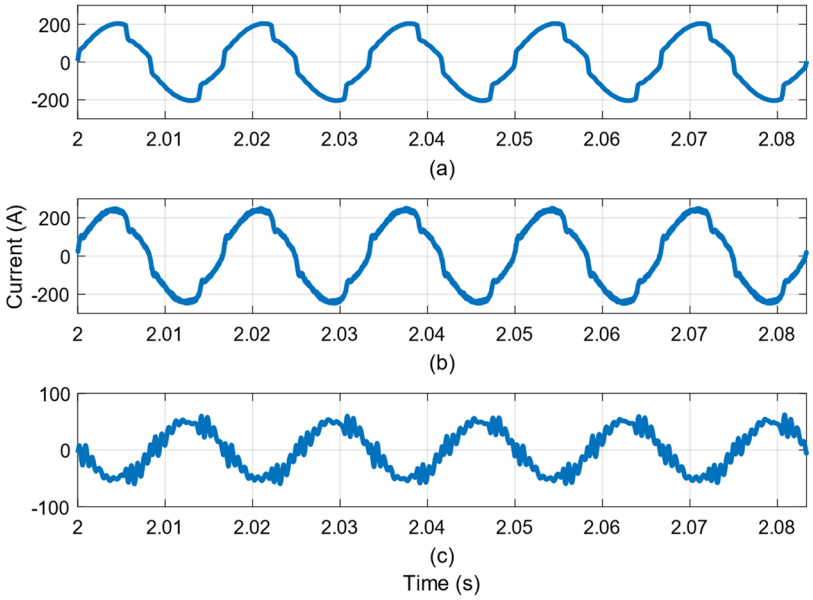


Figure 36. Waveform: (**a**) of the load current, (**b**) of the output current of the photovoltaic generation unit and (**c**) of the PCC.

Looking at Figure 36, it is noticeable that the appearance of the PCC current after harmonic compensation is more like that of a sinusoid compared to the appearance of the load current, thus showing that there has indeed been harmonic current compensation. To validate this, the FFTs of the PCC currents without and with compensation are analyzed, as shown in Figures 37 and 38.

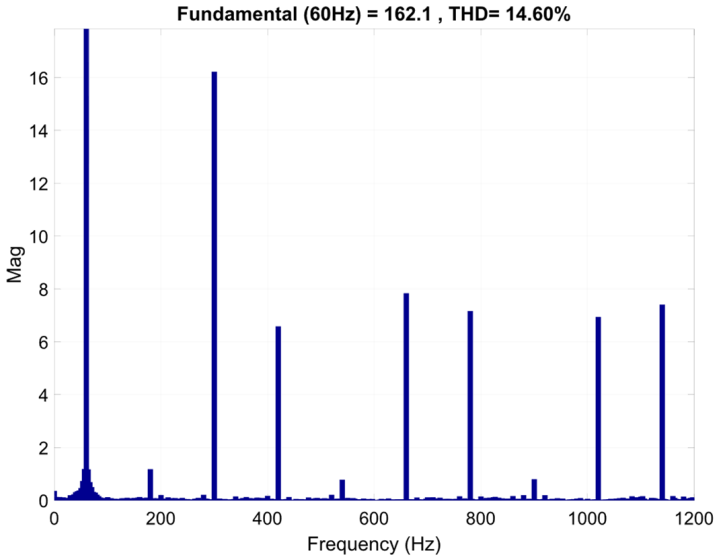


Figure 37. FFT of PCC current without compensation.

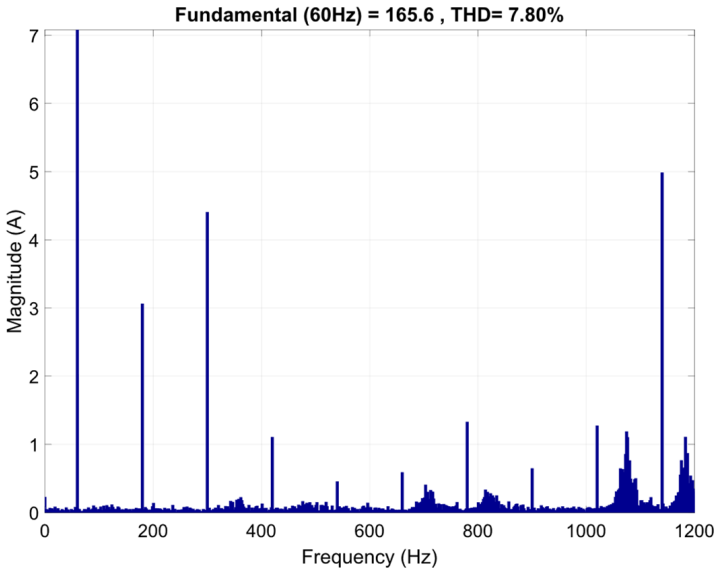


Figure 38. FFT of PCC current with compensation.

As can be seen in Figures 37 and 38, the THD of the PCC current after compensation has been halved, for a similar fundamental current. In addition, when evaluating the frequency components, high attenuation can be seen at all frequencies that have resonant controllers in the DC/AC converter, thus validating the compensation of harmonic currents.

In relation to harmonic compensation, the performance of the compensation was also evaluated in the face of power fluctuations on the DC side of the converter. To do this, the DG was simulated with approximately 10% photovoltaic generation and the storage system was tasked with making up for this generation shortfall. Table 7 shows the amplitude of the frequency components compensated by the control system with the converter operating at nominal power and partial power.

Table 7. Magnitude and phase values for the system with and without resonant portions.

Harmonic Order	Frequency (Hz)	Magnitude (A)	
		Partial Power	Nominal Power
5th	300	4.5	4.4
7th	420	1.1	1.25
11th	660	0.7	0.7
13th	780	1.25	1.15
17th	1020	1.23	1.1
19th	1140	5	4.5

The data in Table 7 shows that there are no major variations in the compensation of harmonic currents with the DC/AC converter operating at partial power in relation to the rated power, since the frequency components of the compensated PCC current remained close to the rated power.

Through the harmonic compensation carried out by the DC/AC converter, it was possible to attenuate the current harmonics coming from a non-linear load. This compensation is useful in electrical systems, as it avoids the consequences of these unwanted signals.

6. Discussion

With regard to frequency support, the presence of an energy storage system in a photovoltaic generating unit plays a fundamental role in stabilizing the electrical system. It helps to smooth out fluctuations in generation, attenuate frequency oscillations and can make the system's response resemble that of a system with greater inertia, as seen in Figures 27 and 28. This is important information for planning and operating power systems with a significant share of photovoltaic generation. Furthermore, the effectiveness of this system depends on several factors, including the statics selected, the PLL algorithm and the converter controllers, as seen in Figures 29 and 30. In general, however, the storage system helps to reduce power fluctuations, improving stability in relation to fluctuations in photovoltaic generation.

With terms of reactive power support, the renewable energy generation unit was able to adjust its operation to meet a request to dispatch maximum reactive power to the detriment of active power. This is done by directing all the photovoltaic generation power to the energy storage system, demonstrating flexibility in the operation of the generating unit, as shown in Figure 32a–c. This capacity to respond is important for supporting the stability and power quality on the grid, especially when it is necessary to supply or absorb reactive power to keep the voltage within the appropriate limits. Also noteworthy is the ability of batteries to store the energy generated by the photovoltaic system when there is excess reactive generation by the inverter. This can be beneficial for the stability and efficiency of the power system.

With relation to active power dispatch and regulation of the PCC load curve, it is worth mentioning the behavior of the energy storage system in relation to power demand, highlighting the importance of strategies such as active power dispatch and charging at strategic times to optimize the system (load relief) and increase its efficiency in serving local loads. In addition, the stability of the grid must be considered when connecting distributed generation units. The presence of abrupt power variations can be a challenge, but the incorporation of ancillary services can help maintain grid stability by preventing overloads, frequency and voltage instability through the regularization of the load curve, as shown in Figure 35. This highlights the importance of proper planning and advanced technology to deal with the complexities of integrating renewable energy sources into the grid.

Therefore, in relation to the compensation of harmonic currents in the PCC, the effectiveness of DG with harmonic compensation control in improving the power quality is evident. This was confirmed by observing that the current in the PCC became more like a

sinusoid after compensation, indicating a significant reduction in harmonics, as illustrated in Figure 36a–c. Therefore, the evaluation was carried out both in situations with low dispatched power and in situations with nominal power values. This implies that the harmonic compensation capability was tested under different load conditions, which is relevant for verifying its effectiveness in a variety of scenarios, as shown in Table 7. Given this situation, there was a significant reduction in current THD, in which the maintenance of the fundamental current and the attenuation of resonant frequencies indicate that the compensation was effective, as corroborated by Figures 37 and 38. In addition, the ability to cope with oscillations in photovoltaic generation shows the robustness of the compensation system in dynamic situations.

Finally, it is worth pointing out that the method proposed in this work for the joint operation of several extra functions in a hybrid photovoltaic inverter has some limitations, which must be taken into account. One of these is in relation to frequency and reactive power support. The limitation lies in the dynamics of the response of these systems, since this is determined by the dynamics of the variation in frequency and voltage of the grid, and it is not possible to change it, since only one gain is used to obtain the final response (frequency and voltage droop in steady state). The second limitation is harmonic compensation. It is worth noting that, although the harmonic components have a high level of attenuation, they have not been completely eliminated, thus demonstrating the limitations of this function.

7. Conclusions

Therefore, based on the study carried out, the possibility of performing ancillary services such as frequency support, reactive power support, active power dispatch, load curve regulation and PCC harmonic current compensation was verified. These services were evaluated from the point of view of simultaneous execution with the conventional operation of the generating unit.

In this sense, the simulation results obtained demonstrate the technical viability from the point of view of the system's operation, since it was operated at all times within its nominal limits. In addition, the effectiveness of the services provided stands out, as improvements over the conventional system were observed. It is also worth highlighting the joint operation of the battery energy storage system with the photovoltaic generating unit integrated into a single DC/AC converter. This integration allows for greater flexibility in terms of power flow between generation and the storage system, as well as greater efficiency when compared to systems that operate separately.

As a proposal for future work, it is recommended that the system be studied using control models that integrate virtual synchronous machine systems, as this would tend to improve the efficiency of the frequency support in the face of disturbances. It is also worth noting that the reactive power dispatch strategy can be improved to inject power into unbalanced systems, in order to improve the voltage indices per phase. Finally, it is worth highlighting the need for experimental validation of the proposed system.

Author Contributions: L.T.F.S. and Souza, A.C.d.S. designed the study, performed the experiments, and wrote the manuscript; L.F.P. and G.H.A. contributed to the experiments and elaborated the manuscript; W.W.A.G.S. and A.C.d.S. contributed project organization and administration. All authors have read and agreed to the published version of the manuscript.

Funding: This work was financially supported in part by the Notice 06/2023 - Support for New Researchers - designated by the research directorate (DIP) of UNIFEI - Universidade Federal de Itajubá campus Itabira, and in part by the following Brazilian research funding agencies: Fundação de Amparo à Pesquisa do Estado de Minas Gerais (FAPEMIG).

Data Availability Statement: Not applicable.

Acknowledgments: The authors would like to thank the Research Support Fundação de Amparo à Pesquisa do Estado de Minas Gerais (FAPEMIG).

Conflicts of Interest: The authors declare no conflict of interest.

Appendix A

Table A1 demonstrates the parameter values of the algorithms and controllers used in the computational implementation.

Table A1. Values of parameters used in the computational implementation.

Application	Parameter	Value
Boost Controller	kp_{ib}	0.0232
	ki_{ib}	0.4189
	kp_{vb}	−0.0034
	ki_{vb}	−27.6554
Buck-Boost Controller	kp_{ibt}	0.0255
	ki_{ibt}	0.4189
DC/AC Converter Controller	kp_{i}	3.7806
	ki_{i}	188.4956
	kp_{v}	−60.1195
	ki_{v}	−590.2220
	kp_{q}	-1.0206×10^{-4}
	ki_{q}	−0.6413
Active power relief algorithm	ω_{min}	376.99
	ω_{max}	377.02
	SOC_{min}	20
	SOC_{max}	99.99
Resonant Controller	K_{ih}	4.189
	ω_{c}	1

References

1. Casamali, D.F.; de Aquino, A.F.d.C.; e Silva, A.S. Supplementary Frequency Control for Low Inertia Power Systems. *J. Control Autom. Electr. Syst.* **2023**. [CrossRef]
2. Kurita, Y.; Moriya, Y.; Kakisaka, H.; Iwamoto, S. A novel LFC scheme using storage battery control and generator feed-forward control for large-scale wind power penetration. In Proceedings of the 2016 IEEE Region 10 Conference (TENCON), Singapore, 22–25 November 2016; IEEE: Piscataway, NJ, USA, 2016; pp. 3332–3335.
3. Nguyen, H.T.; Yang, G.; Nielsen, A.H.; Jensen, P.H. Combination of synchronous condenser and synthetic inertia for frequency stability enhancement in low-inertia systems. *IEEE Trans. Sustain. Energy* **2018**, *10*, 997–1005. [CrossRef]
4. Chamorro, H.R.; Torkzadeh, R.; Eliassi, M.; Betancourt-Paulino, P.; Rezkalla, M.; Gonzalez-Longatt, F.; Sood, V.K.; Martinez, W. Analysis of the gradual synthetic inertia control on low-inertia power systems. In Proceedings of the 2020 IEEE 29th International Symposium on Industrial Electronics (ISIE), Delft, The Netherlands, 17–19 June 2020; IEEE: Piscataway, NJ, USA, 2020; pp. 816–820.
5. Li, X.; Ma, R.; Wang, L.; Wang, S.; Hui, D. Energy management strategy for hybrid energy storage systems with echelon-use power battery. In Proceedings of the 2020 IEEE International Conference on Applied Superconductivity and Electromagnetic Devices (ASEMD), Tianjin, China, 16–18 October 2020; IEEE: Piscataway, NJ, USA, 2020; pp. 1–2.
6. Tu, L.; Yang, Y.; Yang, J.; Sun, T. The synthetic inertia controller for mmc-hvdc based offshore wind farm integration. In Proceedings of the 2021 IEEE 1st International Power Electronics and Application Symposium (PEAS), Shanghai, China, 13–15 November 2021; IEEE: Piscataway, NJ, USA, 2021; pp. 1–4.
7. Egwebe, A.M.; Fazeli, M.; Holland, P. Adaptive virtual resistance load sharing for resistive microgrids. *Electr. Power Syst. Res.* **2018**, *160*, 17–26. [CrossRef]
8. Han, H.; Hou, X.; Yang, J.; Wu, J.; Su, M.; Guerrero, J.M. Review of power sharing control strategies for islanding operation of AC microgrids. *IEEE Trans. Smart Grid* **2016**, *7*, 200–215. [CrossRef]
9. Yazdani, A.; Iravani, R. *Voltage-Sourced Converters in Power Systems: Modeling, Control, and Applications*; Wiley: Hoboken, NJ, USA, 2010.

10. Almutairi, S.; Miao, Z.; Fan, L. Stability analysis of two types of grid-forming converters for weak grids. *Int. Trans. Electr. Energy Syst.* **2021**, *31*, e13136. [CrossRef]
11. Han, Y.; Li, H.; Shen, P.; Coelho, E.A.A.; Guerrero, J.M. Review of active and reactive power sharing strategies in hierarchical controlled microgrids. *IEEE Trans. Power Electron.* **2017**, *32*, 2427–2451. [CrossRef]
12. Han, Y.; Shen, P.; Zhao, X.; Guerrero, J.M. An enhanced power sharing scheme for voltage unbalance and harmonics compensation in an islanded AC microgrid. *IEEE Trans. Energy Convers.* **2016**, *31*, 1037–1050. [CrossRef]
13. Akagi, H.; Watanabe, E.H.; Aredes, M. *Instantaneous Power Theory and Applications to Power Conditioning*; Wiley: Hoboken, NJ, USA, 2017.
14. Soares, L.T.F.; Souza, A.C.; Piccini, A.R.; Santos, I.N. Control proposal for photovoltaic inverters with reactive power supply for voltage stability during momentary sags and in steady state. *IEEE Lat. Am. Trans.* **2023**, *21*, 1007–1014. [CrossRef]
15. Serban, I.; Marinescu, C. Battery energy storage system for frequency support in microgrids and with enhanced control features for uninterruptible supply of local loads. *Int. J. Electr. Power Energy Syst.* **2014**, *54*, 432–441. [CrossRef]
16. da Silva Junior, D.C.; Musse, B.F.; Lanes, M.M.; de Oliveira, J.G. Real Time Simulation of Dynamic voltage restorer (DVR) utilizing RTDS and dSPACE. In Proceedings of the 2017 IEEE 8th International Symposium on Power Electronics for Distributed Generation Systems (PEDG), Florianopolis, Brazil, 17–20 April 2017; IEEE: Piscataway, NJ, USA, 2017; pp. 1–8.
17. Hossain, M.A.; Pota, H.R.; Hossain, M.J.; Blaabjerg, F. Evolution of microgrids with converter-interfaced generations: Challenges and opportunities. *Int. J. Electr. Power Energy Syst.* **2019**, *109*, 160–186. [CrossRef]
18. Guerrero, J.M.; Chandorkar, M.; Lee, T.L.; Loh, P.C. Advanced control architectures for intelligent microgrids-part i: Decentralized and hierarchical control. *IEEE Trans. Ind. Electron.* **2013**, *60*, 1254–1262. [CrossRef]
19. Padullaparti, H.V.; Ganta, N.; Santoso, S. Voltage regulation at grid edge: Tuning of PV smart inverter control. In Proceedings of the 2018 IEEE/PES Transmission and Distribution Conference and Exposition (T&D), Denver, CO, USA, 16–19 April 2018; IEEE: Piscataway, NJ, USA, 2018; pp. 1–5.
20. da Silveira Postiglione, C.; Simoes, M.G. dSPACE based implementation of a grid connected smart inverter system. In Proceedings of the 2010 IEEE 12thWorkshop on Control and Modeling for Power Electronics (COMPEL), Boulder, CO, USA, 28–30 June 2010; IEEE: Piscataway, NJ, USA, 2010; pp. 1–5.
21. Ding, F.; Nguyen, A.; Walinga, S.; Nagarajan, A.; Baggu, M.; Chakraborty, S.; McCarty, M.; Bell, F. Application of autonomous smart inverter volt-var function for voltage reduction energy savings and power quality in electric distribution systems. In Proceedings of the 2017 IEEE Power & Energy Society Innovative Smart Grid Technologies Conference (ISGT), Washington, DC, USA, 23–26 April 2017; IEEE: Piscataway, NJ, USA, 2017; pp. 1–5.
22. Abate, S.; McDermott, T.; Rylander, M.; Smith, J. Smart inverter settings for improving distribution feeder performance. In Proceedings of the Proceedings of the 2015 IEEE Power & Energy Society General Meeting, Denver, CO, USA, 26–30 July 2015; IEEE: Piscataway, NJ, USA, 2015; pp. 1–5.
23. Harirchi, F.; Simões, M.G.; Babakmehr, M.; Al-Durra, A.; Muyeen, S. Designing smart inverter with unified controller and smooth transition between grid-connected and islanding modes for microgrid application. In Proceedings of the 2015 IEEE Industry Applications Society Annual Meeting, Addison, TX, USA, 18–22 October 2015; IEEE: Piscataway, NJ, USA, 2015; pp. 1–7.
24. Jafarian, H.; Kim, N.; Parkhideh, B.; Enslin, J. Analysis of smart inverter functions of decentralized grid-connected AC-stacked PV inverter architecture. In Proceedings of the 2017 IEEE Applied Power Electronics Conference and Exposition (APEC), Tampa, FL, USA, 26–30 March 2017; IEEE: Piscataway, NJ, USA, 2017; pp. 3594–3600.
25. Júnior, D.C.S.; de Santiago, J.; de Almeida, P.M.; Oliveira, J.G. Control of Smart Inverters with Automated Decisions in Microgrid. *J. Control Autom. Electr. Syst.* **2023**, *34*, 1028–1042. [CrossRef]
26. Ranjbaran, A.; Ebadian, M. A power sharing scheme for voltage unbalance and harmonics compensation in an islanded microgrid. *Electr. Power Syst. Res.* **2018**, *155*, 153–163. [CrossRef]
27. Online Document, IEEE PES Test Feeder. Available online: https://cmte.ieee.org/pes-testfeeders/resources/ (accessed on 11 January 2023).
28. Yanarates, C.; Zhou, Z. Design and Cascade PI Controller-Based Robust Model Reference Adaptive Control of DC-DC Boost Converter. *IEEE Access* **2022**, *10*, 44909–44922. [CrossRef]
29. Souza, A.C.; Melo, F.C.; Oliveira, T.L.; Tavares, C.E. Performance Analysis of the Computational Implementation of a Simplified PV Model and MPPT Algorithm. *IEEE Lat. Am. Trans.* **2016**, *14*, 792–798. [CrossRef]
30. Ogata, K. *Modern Control Engineering*, 5th ed.; Prentice-Hall: Upper Saddle River, NJ, USA, 2010.
31. Tremblay, O.; Dessaint, L.-A.; Dekkiche, A.-I. A Generic Battery Model for the Dynamic Simulation of Hybrid Electric Vehicles. In Proceedings of the 2007 IEEE Vehicle Power and Propulsion Conference, Arlington, TX, USA, 9–12 September 2007; pp. 284–289. [CrossRef]
32. MATHWORKS®-MATLAB. Battery: Generic Battery Model. Available online: https://www.mathworks.com/help/sps/powersys/ref/battery.html (accessed on 29 August 2023).
33. Barater, D.; Concari, C.; Buticchi, G.; Gurpinar, E.; De, D.; Castellazzi, A. Performance Evaluation of a Three-Level ANPC Photovoltaic Grid-Connected Inverter With 650-V SiC Devices and Optimized PWM. *IEEE Trans. Ind. Appl.* **2016**, *52*, 2475–2485. [CrossRef]
34. Rashid, M.H. *Eletrônica de Potência: Dispositivos, Circuitos e Aplicações*, 4th ed.; São Paulo: Pearson, FL, USA, 2014.

35. Blaabjerg, F.; Iov, F.; Teodorescu, R.; Chen, Z. Power electronics in renewable energy systems. In Proceedings of the Power Electronics and Motion Control Conference, Portoroz, Slovenia, 30 August–1 September 2006; pp. 1–17.
36. Rodriguez, P.; Pou, J.; Bergas, J.; Candela, J.I.; Burgos, R.P.; Boroyevich, D. Decoupled Double Synchronous Reference Frame PLL for Power Converters Control. *IEEE Trans. Power Electron.* **2007**, *22*, 584–592. [CrossRef]
37. Liserre, M.; Blaabjerg, F.; Hansen, S. Design and control of an LCL-filter-based three-phase active rectifier. *IEEE Trans. Ind. Appl.* **2005**, *41*, 1281–1291. [CrossRef]
38. Chapman, S.J. *Fundamentos de Máquinas Elétricas*, 5th ed.; AMGH: Porto Alegre, Brazil, 2013; 700p.
39. Teodorescu, R.; Blaabjerg, F.; Liserre, M.; Loh, P.C. A new breed of proportional-resonant controllers and filters for grid-connected voltage-source converters. *Proc. Inst. Electr. Eng. Electr. Power Appl.* **2006**, *153*, 750–762. [CrossRef]
40. Chu, Z.; Teng, F. Voltage Stability Constrained Unit Commitment in Power Systems With High Penetration of Inverter-Based Generators. *IEEE Trans. Power Syst.* **2023**, *38*, 1572–1582. [CrossRef]
41. Xiong, L.; Liu, X.; Liu, H.; Liu, Y. Performance Comparison of Typical Frequency Response Strategies for Power Systems With High Penetration of Renewable Energy Sources. *IEEE J. Emerg. Sel. Top. Circuits Syst.* **2022**, *12*, 41–47. [CrossRef]

Disclaimer/Publisher's Note: The statements, opinions and data contained in all publications are solely those of the individual author(s) and contributor(s) and not of MDPI and/or the editor(s). MDPI and/or the editor(s) disclaim responsibility for any injury to people or property resulting from any ideas, methods, instructions or products referred to in the content.